Probing Iceland's Dust-Emitting Sediments: Particle Size Distribution, Mineralogy, Cohesion, Fe Mode of Occurrence, and Reflectance Spectra Signatures

Adolfo González-Romero[1,2,3], Cristina González-Flórez[1,3], Agnesh Panta[4], Jesús Yus-Díez[5], Patricia Córdoba[2], Andres Alastuey[2], Natalia Moreno[2], Konrad Kandler[4], Martina Klose[6], Roger N. Clark[7], Bethany L. Ehlmann[8], Rebecca N. Greenberger[8], Abigail M. Keebler[8], Phil Brodrick[9], Robert O. Green[9], Xavier Querol[2], Carlos Pérez García-Pando[1,10]

[1] Barcelona Supercomputing Center (BSC), Barcelona, Spain
[2] Spanish Research Council, Institute of Environmental Assessment and water Research (IDAEA-CSIC), Barcelona, Spain
[3] Polytechnical University of Catalonia (UPC), Barcelona, Spain
[4] Institute of Applied Geosciences, Technical University Darmstadt, Darmstadt, Germany
[5] Centre for Atmospheric Research, University of Nova Gorica, Ajdovščina, Slovenia.
[6] Karlsruhe Institute of Technology (KIT), Institute of Meteorology and Climate Research Troposphere Research (IMKTRO), Karlsruhe, Germany
[7] PSI Planetary Science Institute, Tucson, AZ, USA
[8] Division of Geological and Planetary Sciences, California Institute of Technology, 1200 E. California Blvd., Pasadena 91125 CA, USA
[9] Jet Propulsion Laboratory, California Institute of Technology
[10] Catalan Institution for Research and Advanced Studies (ICREA), Barcelona, Spain

Corresponding author: Adolfo González-Romero (agonzal3@bsc.es) and Xavier Querol (xavier.querol@idaea.csic.es)

Abstract

Characterizing physico-chemical properties of dust-emitting sediments in arid regions is fundamental to understand the effect of dust on climate and ecosystems. For high-latitude dust (HLD), this knowledge is scarce. This study focuses on the particle size distribution (PSD), mineralogy, cohesion, iron (Fe) mode of occurrence and Visible Near Infra-Red (VNIR) reflectance spectra of dust-emitting sediments from dust-hotspots in Iceland (HLD region). Extensive analysis was conducted on top sediments collected from seven dust-sources and an intensive at Jokulsá basin including top sediments, sediments and aeolian ripples. Fully and minimally dispersed PSDs evidenced remarkable similarities with an average median diameter of 56±69 and 55±62 µm. Mineralogical analyses showed the prevalence of amorphous phases (68±26 %), feldspars (17±13 %), and pyroxenes (9.3±7.2 %), aligned with the reflectance spectra. Fe content reached 9.5±0.40 wt %, mainly in silicate structures (80±6.3 %), complemented by magnetite (16±5.5 %), hematite/goethite (4.5±2.7 %), and readily exchangeable Fe-ions or Fe nano-oxides (1.6±0.63 %). Icelandic top sediments have coarser PSD compared to the high dust-emitting crusts from mid-latitude arid regions, distinctive mineralogy, and threefold bulk Fe content, with a large presence of magnetite. The congruence between fully and minimally dispersed PSDs underscores a reduced particle aggregation and cohesion of Icelandic top sediments, suggesting that aerodynamic entrainment of dust may also play a role upon emission in this region, aside of saltation bombardment. The analysis of an extensive sampling in Dyngjusandur allowed this study to present a conceptual model to encapsulate Iceland's rapidly evolving high dust-emitting environments.

Keywords: Arid regions, Iceland dust-sources, Arctic desert, High latitude dust, Dust modelling

1. Introduction

Dust particles created by wind erosion of arid surfaces can traverse considerable distances, spanning continents and oceans, and influencing the Earth's climate (Kok et al., 2023). The impact of dust on climate and the environment strongly depends upon its shape, particle size distribution (PSD) and composition, which to a large extent are determined by its associated source of sediments (Kok et al., 2023). While most of the dust is produced in hot, arid, subtropical sources like the Sahara, and most studies have concentrated on these regions, but dust produced in cold high-latitude environments, defined as dust emitted from latitudes ≥ 50° N and ≥ 40° S, receives increasing attention due to its regional and potentially global significance (Bullard et al., 2016; Meinander et al., 2022). High-latitude dust (HLD) is emitted from regions as Iceland, Greenland, Svalbard, Alaska, Canada, Antarctica, New Zealand, and Patagonia, and its physical, chemical and optical properties can differ strongly from those of crustal dust produced in lower latitude sources, and affect, among other, atmospheric (Johnson et al., 2010), marine (Jickells et al., 2005), and cryospheric (Oerlemans et al., 2009) processes.

Numerous geophysical processes, especially glacial and periglacial ones, occurring in high latitude regions under current environmental conditions favor the emission of contemporary dust (Bullard, 2013; Bullard et al., 2016). Physical weathering of rocks by glaciers produces a vast amount of silt and sand that is transported from underneath the glacial margins by glacial rivers (Palacios et al., 2022). At a certain point, these glacial rivers flow out from the glacier and form floodplains where the silt and sand are deposited, enabling dust emission to the atmosphere by strong winds. Additionally, in active volcanic regions, massive volumes of volcanic ash can be trapped by ice in glaciers across geological history and be supplied as sediment to the glacial rivers upon melting. Such regions are common in Iceland, and include Dyngjusandur, Skeiðarársandur, Mælifellssandur and Mýrdalssandur (Arnalds et al., 2001). In Iceland, active volcanoes erupt every 3-5 years, depositing thick layers of tephra ranging from millimetres to centimetres (Arnalds et al., 2016). This process has the potential to lead to the formation of new dust sources when new basalt fields obstruct river flows and create ephemeral lakes. All these processes together make Iceland one of the most active dust hotspots in the world, with >20,000 km^2 of sandy deserts (≈20 % of Iceland) exposed to aggressive aeolian activity releasing millions of tonnes of dust to the atmosphere (Arnalds et al., 2016; Baldo et al., 2020). Icelandic dust is emitted, transported and deposited over land, sea, and ice of the North Atlantic, covering areas in Iceland, north-western Europe, north-eastern America and Greenland (Arnalds et al., 2014; Baldo et al., 2020). Icelandic dust can reduce surface albedo and either increase or decrease melting of glaciers and ice caps via deposition depending on the deposited layer thickness (Dragosics et al., 2016; Wittmann et al., 2017; Möller et al., 2016, 2018). Icelandic dust is also rich in iron (Fe) (e.g. Arnalds et al., 2014), which depending on its mode of occurrence can exert different climate and ecological effects. Fe-oxide minerals strongly absorb solar radiation (Formenti et al., 2014; Engelbrecht et al., 2016; Di Biagio et al., 2019; Zubko et al., 2019), potentially contributing to direct radiative effects in the Arctic (Kylling et al., 2018). The deposition of soluble Fe from Icelandic dust to the ocean can impact Fe biogeochemistry and primary productivity in the subpolar North Atlantic Ocean, which is seasonally Fe limited (Arnalds et al., 2014). Icelandic dust can also be a sporadically important source of ice-nucleating particles (INP) at mid to high latitudes (Sanchez-Marroquin et al., 2020; Shi et al., 2022), relevant to the cloud-phase climate feedback (Murray et al., 2021).

Desert dust can also affect air quality, and accordingly human health (Goudie & Middleton, 2006; De Longeville et al., 2010; Karanasiou et al., 2012; Pérez García-Pando et al., 2014). Thorsteinsson et al.

129 (2011) reported ambient concentrations of atmospheric particulate matter (PM) <10 µm (PM_{10}) higher
130 than 100 µg/m^3, on a 30 min basis, during various dust storms in Reykjavik, with dust transport from
131 the Landeyjarsandur area (100 km ESE of the capital). Dagsson-Waldhauserova et al. (2016) reported
132 mean 5 minutes averages PM_{10} and PM_1 levels of 158-583 and 97-241 µg/m^3, respectively at
133 Landeyjarsandur, and 7-486 µg/m^3 PM_{10} at Hagavatn (both major dust hotspots). Dagsson-
134 Waldhauserova et al. (2015) reported similar PM_{10} levels in Reykjavik, but higher in
135 Kirkjubæjarklaustur (up to 6500 µg/m^3, 1 min basis).

136 Dyngjusandur, Dyngjuvatn, Hagavatn, Mælifellsandur, Mýrdalssandur, Landeyjarsandur and
137 Skaftarsandur (Figure 1) are the most active dust emission areas in Iceland (Arnalds, 2020). The
138 emission of dust in these regions depends on the season. In the long cold periods, the snow cover
139 prevents dust emissions (Arnalds, 2010). After thawing, the soils have too much moisture to be able
140 to emit; nonetheless, during summer (mostly August) there is a higher probability for dust emission,
141 especially in inland areas, such as Dyngjusandur (Figure 1), where the periodic passage of fronts from
142 the Arctic and low pressure systems are common and are associated with high winds, generally
143 between 5 and 15 m/s, with peaks of up to 30 to 50 m/s, 10 m height (Einarsson, 1984, Olafsson et al.,
144 2007).

145 Glaciofluvial sediments in Iceland may exhibit distinct particle size characteristics. Samples collected
146 in Dyngjusandur, Hagavatn, Landeyjarsandur, Maelifellsandur, Myrdahlsandur, and Sandkluftavatn
147 generally display unimodal distributions with a notably diverse profile, featuring average diameters
148 ranging from 20 to 98 µm (Meinander et al., 2022). Icelandic dust is mostly made up of basaltic
149 particles (Baratoux et al., 2011; Thorpe et al., 2019). The dust emitting sediments mainly consist of
150 volcanic glass (up to 80-90 %, except for some dust hotspots, such as Hagavatn, with <40 %), with
151 minor proportions of anorthite (0-20 %), augite (0-10 %), and traces of forsterite, microcline, Ti-
152 magnetite and quartz (Baldo et al., 2020). Wada et al. (1992), reported the occurrence of plagioclase,
153 augite, halloysite, allophane and imogolite in sediment samples at Thingvallasveit, Myrdalur,
154 Biskupstungnaafrettur and Godafoss; while Thorpe et al. (2019) that of plagioclase, augite, olivine,
155 volcanic glass and secondary minerals in soil samples at Hvítá. Baratoux et al. (2011) reported that
156 dust near Dyngjusandur was made up of 80-90 % of volcanic glass, and traces of pyroxene, olivine and
157 plagioclase, and that from Lambrahaun was made up of 0-20 % of volcanic glass with very high
158 plagioclase and olivine contents. Dagsson-Waldhauserova et al. (2015) showed that a deposited dust
159 sample from a top snow layer in Reykjavik reflected the major basaltic composition of the source
160 lands, with mean values of 40-50 % SiO_2, 14-20 % Al_2O_3, 8-16 % CaO, 2-4 % Na_2O + K_2O, 4-9 % MgO,
161 10-17 % FeO and 0.8-5 % of TiO_2, which is in concordance with that of PM_{10} and PM_{20} obtained by
162 resuspension of sediment samples in a chamber (Baldo et al. 2020). Dagsson-Waldhauserova et al.
163 (2015) also showed that deposited dust from Mælifellsandur and Skeidarársandur were similar in
164 composition, with 42-45 % SiO_2, 14-15 % Al_2O_3, 11-12 % CaO, 4.0-4.1 % Na_2O + K_2O, 4.9-6.2 % MgO,
165 14-17 % FeO and 3.5-5.6 % of TiO_2.

166 Several atmospheric modelling studies have already attempted at representing HLD (Thorsteinsson et
167 al., 2011; Groot Zwaaftink et al., 2017; Beckett et al., 2017; Cvetkovic et al., 2022; Meinander et al.,
168 2022). However, the inclusion of HLD in Earth system models is only at its early stages (Shi et al., 2022),
169 and it is currently a challenge. While the fundamental processes governing aeolian dust emissions in
170 HLD should be broadly consistent with those in temperate regions, many HLD source regions exhibit

additional or amplified processes unique to their environment. These include the highly dynamic nature of many of its sources, their potential expansion driven by glacier melting and retreat in a warming climate (Meinander et al., 2022), the emission mechanisms and its distinct physicochemical properties. Currently, there is a lack of information on the PSD and mineralogy of dust sources to feed model simulations of emission and transport of dust for climate and environmental impact assessment (Laurent et al., 2008; Perlwitz et al., 2015a and b; Kok et al., 2021). This is especially evident for HLD, where dust observations are scarce (Cvetkovic et al., 2022) and mineralogical maps for dust modelling are not available (Claquin et al., 1999; Journet et al., 2014; Green et al., 2020). Specifically, the size and mode of occurrence of Fe require investigation (Mahowald et al., 2005). It is known that hematite/goethite increases the radiative forcing of dust whereas nano Fe-oxides and easily exchangeable Fe might increase the fertilising effect of dust in ocean and terrestrial ecosystems (Baldo et al., 2020). However, magnetite has different wavelength-dependent optical properties than hematite/goethite (Matsui et al., 2018), and for Icelandic dust it might be the principal contributor to its radiative absorption effect on climate. Also, the high proportions of volcanic glass can influence the radiative forcing of Icelandic dust (Baldo et al., 2023). All in all, there is a pressing need for an improved understanding of the formation and distribution of sediments in HLD hotspots, encompassing an in-depth examination of their compositional and physical attributes. Specifically, a characterization of the PSD, mineral composition, the mode of occurrence of Fe and Visible Near Infra-Red (VNIR) reflectance spectral signatures is essential for accurate representation of HLD sources and the associated dust effects in forthcoming Earth System models. The analysis of both minimally disturbed PSD (MDPSD) and fully disturbed PSD (FDPSD) can further help in understanding the degree of particle aggregation and sediment cohesion (González-Romero et al., 2023), which should contribute towards understanding and constraining dust emission schemes in these regions.

This study aims at investigating the major patterns of sediments and processes that account for the high dust emission in Dyngjusandur (Figure 1), one of the most active dust emission areas in Iceland and, more generally, in HLD sources. The major focus is to understand the geological controls for sediment accumulation, while characterizing the mineralogical composition, PSD, mode of occurrence of Fe, degree of cohesion and VNIR reflectance spectra of the dust-emitting sediments in the Jokulsá á fjöllum basin from Vatnajökull (front of the glacier) to Holuhraun (lava field in the middle of the basin) and towards the sea (Figure 1). As a result, a conceptual model for the accumulation of fine-grained sediments and dust emission in the region is elaborated. Additionally, the analysis of samples from other prominent Icelandic dust sources, including Dyngjuvatn, Hagavatn, Landeyjasandur, Mælifellsandur, Mýrdalssandur and Skaftarsandur (Figure 1), are used to evaluate to what extent sediment properties differ across Icelandic dust-hotspots. Finally, the properties of Iceland's dust emitting-sediments are compared with those from a hotspot recently analysed with the same techniques in the Moroccan Sahara (González-Romero et al., 2023).

2. Methodology

2.1 FRAGMENT field campaigns

This study is part of the FRontiers in dust minerAloGical coMposition and its Effects upoN climaTe (FRAGMENT) project. FRAGMENT has performed a set of coordinated and interdisciplinary field campaigns over remote dust sources in Morocco (2019), Iceland (2021), United States (2022) and

212 Jordan (2022). The project aims to better understand and quantify the properties of dust-source
213 sediments and their relationship to the properties of the emitted dust, evaluate and improve ongoing
214 spaceborne spectroscopy retrievals of surface minerals and improve the Earth system model
215 representation of dust mineralogy. The FRAGMENT campaigns in Morocco, Iceland and Jordan
216 included detailed regional sediment sampling along with an intensive wind erosion and dust emission
217 intensive measurement campaign in one location (e.g., in Morocco, see González-Romero et al., 2023,
218 González-Florez et al., 2023; Panta et al., 2023; Yus-Díez et al., in prep/in submission 2023). The
219 FRAGMENT campaign in the US included sediment sampling only.

220 This study reports the results from the sediment sampling carried out in the Dyngjusandur basin and
221 other dust emission hotspots in Iceland. The intensive wind erosion and dust emission field campaign
222 took place in Dyngjusandur, 300 m away from the newest parts of the Holuhraun lava field, where
223 Jökulsá water flow is accumulated after flash floods, creating an endorheic lake. The results of the
224 intensive field campaign will be presented in forthcoming studies.

225 2.2 Study site

226 In northern Iceland, in the Jokulsá á Fjöllum basin, Dyngjusandur has been reported as the largest and
227 most active dust-emitting area by Arnalds et al. (2010) (Figure 1). The glacier Vatnajökull is the source
228 of sand, silt and clay size particles that are transported northwards through the Jökulsá á Fjöllum river
229 and tributaries as Kreppa, Arnardalsá and Skardsá, to the sea (Figure 1). The Bárðarbunga eruption
230 and the Holuhraun lava field cut the basin flow 16 km away from Vatnajökull, forming the ephemeral
231 Dyngjusandurvatn lake (referred in this study as Dyngjusandur), which is affected by flooding
232 recurrently every summer (Figure 1). The ponded waters are filtered through the Holuhraun lava field,
233 connecting again after the lava field with the Jokulsá á Fjöllum river (Arnalds et al., 2016), and allows
234 the deposition of fresh sediments at Dyngjusandur, which can emit dust under favourable conditions.
235 Sediment samples were collected along the river to characterise the variability of the particle size and
236 composition of sediments from the Vatnajökull moraine itself (front moraine) down to the sea (Jokulsá
237 á Fjöllum basin), with an exhaustive sampling that aimed to better characterise sediments from this
238 dust-emission hotspot, located in the surroundings of the Dyngjusandur lake, before the Holuhraun
239 lava field (Figure 1). Furthermore, other dust-emitting sediments were collected in different hotspot
240 sources around Iceland, including Dyngjuvatn (an endorheic lake near the Jókulsá á Fjöllum basin but
241 not connected to it and not to be confused with Dyngjusandur), Hagavatn (an ephemeral lake where
242 sediments pond, sediment and sort), Skaftarsandur (riverine sediments near the sea coast),
243 Landeyjarsandur (riverine sediments that flow towards the ocean and deposit), Mælifellsandur (a river
244 that surrounds the glacier and contributes with fresh sediment) and Mýrdalssandur (riverine
245 sediments on a wide riverbed) (Figure 1).

246 2.3 Sampling

247 The samples collected are representative of surfaces that can be found in the dust-emitting and sandy
248 areas over Iceland. These include the top first centimetre (top sediment in this study) of freshly
249 deposited sediments from dust-emission hotspots, underlying sediments (fluvial sediments in this
250 study), and aeolian ripples found near and around these hotspots (Figure 2). We used a metallic
251 shovel, the same as in González-Romero et al. (2023), of about 5 cm^2 and 2 cm height to sample, and
252 we also noted coordinates, photos of location and area and characteristics of the sample. Samples

253   were stored in plastic bags and transported to the laboratory. Once in the laboratory, samples were
254   dried for 24-48 h at 50 °C and riffled into smaller equal and homogeneous sub-samples for further
255   treatments and analysis.

2.4 Analyses

256

257   ### 2.4.1 Particle size distribution
258   Particle size distributions (PSDs) were analysed through fully dispersed (natural aggregates totally
259   dispersed, as much as possible through a dispersion shaking) and minimally dispersed methods
260   (natural aggregates minimally dispersed, dry measurements) according to González-Romero et al.
261   (2023). A coarser minimally dispersed PSD would indicate high aggregation, while similarity between
262   the minimally and totally dispersed PSDs would indicate a low aggregation of particles in dust-emitting
263   sediments; this has key implications for the mechanisms of dust emission. In both cases, PSDs were
264   determined by laser diffraction with a Malvern Mastersizer 2000 Scirocco and a Hydro G accessories,
265   for minimally and fully dispersed conditions, respectively. In the totally dispersed conditions, we
266   followed the procedure presented in Sperazza et al. (2004).

267   ### 2.4.2 Mineralogical composition
268   X-Ray Diffraction (XRD), coupled with the Rietveld method, has been increasingly used as a fast and
269   reliable method to evaluate the content of the crystalline and amorphous phases in inorganic
270   materials (Rietveld, 1969; Cheary and Coelho, 1992; Young, 1993 and Topas, 2018). Quantification of
271   mixtures via the Rietveld method is generally restricted to crystalline phases for which structures are
272   well known. However, the addition of a known amount of an internal standard material allows the
273   quantification of any amorphous (non-crystalline) material in the mixture that has not been included
274   in the model, in our case, volcanic glass (De la Torre et al., 2001; Madsen, 2001, Scarlett and Madsen,
275   2006; Machiels et al., 2010; Ibañez et al., 2013). Sample preparation for quantitative mineralogical
276   analysis consisted of preliminary dry grinding of the samples in an agate mortar, mixed with a known
277   amount (10-20 %) of CaF_2 powder (Merck), as an internal standard to allow the determination of
278   amorphous contents, and finally dry grounded again to reduce the grain size distribution and
279   homogenise the mixture. The analysis was carried out by a Bruker D8 A25 Advance powder X-ray
280   diffractometer equipped with a LynxEye 1D position sensitive detector, monochromatic Cu Kα
281   radiation (λ =1,5405 Å) operating at 40 kV and 40 mA. The diffractograms were recorded by scanning
282   from 4º to 120º of 2θ with a step size of 0.015º and a counting time of 1s/step maintaining the sample
283   in rotation (15/min). The mineral identification was performed by searches and comparisons of the
284   patterns from International Centre for Diffraction Database (ICDD, PDF-2) using DIFFRAC.EVA software
285   package (Bruker AXS). The quantitative analysis of the mineral phases was carried out by Rietveld full-
286   pattern analyses performed with the TOPAS 5 software (Bruker AXS), which uses least-square
287   procedures to minimise the differences between the observed and calculated diffractograms. The
288   abundances of the crystalline and amorphous phases were normalised to 100 %wt (weight
289   percentage). The quality of the fitting was evaluated by visually comparing the observed and
290   calculated diffractograms to achieve a realistic model and checking the residual factors (R_B, R_{wp}, R_{exp})
291   and goodness of fit (GOF) calculated by the TOPAS model (Rietveld, 1969; Toby, 2006).

292   2.4.3 Mode of occurrence of Fe

293   The samples were subjected to a series of sequential extractions (Figure S1) aimed at quantifying the

294   content of Fe, including readily exchangeable Fe, hematite and goethite, magnetite, as well as, Fe

295   bearing minerals and volcanic glass. Initially, a portion of each collected sample was subject to

296   duplicate acid digestion using a specialised two-step acid digestion method (Figure S1a) (Querol et al.

297   1993, 1997). This process was employed to ascertain the total Fe content. To validate the accuracy of

298   the analytical and digestion methods, reagent blanks and the standard reference materials NIST SRM

299   1633b (FA) were also subject to digestion. The determination of readily exchangeable Fe ions and

300   nano Fe-oxides, the quantification of crystalline Fe-oxides as hematite and goethite, and the

301   assessment of crystalline magnetite, were all conducted using the laboratory-based sequential

302   extraction method described by Shi et al. (2009) and Baldo et al. (2020). The initial sequential

303   extraction step involved combining 30 mg of the sample with 10 ml of the first extractant solution

304   (ascorbate solution as described in Figure S1b). The mixture was agitated for a period of 24 hours in a

305   light-controlled environment and subsequently filtered. Following this, another 30 mg of the same

306   samples underwent leaching with 10 ml of the second extraction solution (dithionite solution as

307   described in Figure S1c), with 2 hours of shaking under in a light-controlled environment, followed by

308   filtration. The solid residue resulting from this latter extraction was once again leached in a light-

309   controlled environment, this time using 10 ml of a third extraction solution (oxalate solution as

310   described in Figure S1d) and was shaken for a duration of 6 hours before undergoing another filtration.

311   The quantification of the dissolved Fe in each of the three solutions, as well as the bulk acidic digestion,

312   was performed using Inductively Coupled Plasma Atomic Emission Spectrometry (ICP-AES).

313   The bulk Fe content is referred to as FeT. The Fe that is the extractable from the initial leaching process

314   is denoted as FeA, representing the Fe that is readily exchangeable, as well as the Fe present as nano

315   Fe-oxides. The Fe extracted from the second stage, minus FeA, is referred to as FeD, which

316   corresponds to the Fe content of goethite and hematite. Additionally, the Fe content of the third

317   extraction is referred to as FeM, equivalent to the Fe magnetite content. The sum of FeD and FeM is

318   equivalent to the total Fe present in crystalline Fe-oxides. Finally, the FeT minus the sum of FeA, FeD,

319   and FeM is designated as FeS, representing the content of structural Fe or Fe incorporated within the

320   structure of other minerals, such as pyroxenes, other Fe-bearing minerals, and volcanic glass.

321   For quality control purposes in each laboratory-based sequential extraction, 30 mg of the Arizona Test

322   Dust (ATD; ISO 12103-1, A1 Ultrafine Test Dust; Powder Technology Inc.) was subject to the same

323   extraction procedure. The averaged Fe content of the reference material 1633b was found to be

324   7.6±0.5 % (certified 7.8 %). Furthermore, the average values of the sequential Fe extraction of the ATD

325   reference material were 0.062±0.005, 0.45±0.01, and 0.042±0.002 % for FeA, FeA+FeD and FeM,

326   respectively, while the certified contents are 0.067, 0.48, and 0.047 %, respectively.

327   2.4.4 Scanning electron microscopy

328   Particles from sediment samples were deposited on graphite stubs and sputter coated with C for size,

329   morphology, mineralogy, and aggregate evaluation analysis with a JEOM JSM-7001F SEM-EDX

330   Scanning Electron Microscope (SEM).

331

332

2.5 In-situ and airborne VNIR spectroscopy

Reflectance spectra were measured at 17 sampling locations before and after sample collection using an ASD Fieldspec 3 with contact probe attachment. This instrument measures wavelengths 350-2500 nm with spectral resolutions of 3 nm at 0.7 µm and 10 nm at 1.4 and 2.1 µm. Spectra are measured at 1.4 nm sampling for wavelengths 0.35-1.0 µm and 2 nm for 1.0-2.5 µm but are internally resampled and output with 1 nm spacing. All measurements are relative to Spectralon and corrected for the known reflectance properties of Spectralon. While we measured the subsurface after sampling, we did not use those measurements as the soils were too saturated to see the mineralogy well. Surface spectra are reported and compared with spectral libraries and the literature (e.g., Kokaly et al., 2017), and band depths (Table S1) were calculated for key absorption features following the methods of Clark and Roush (1984).

Additionally, airborne imaging spectrometer (AVIRIS) data operated by NASA/JPL was acquired at the Jokulsá á Fjöllum basin, from the glacier down to Holuhraun lava field during the field campaign. Three AVIRIS scenes with 224 contiguous channels of 10 nm and a wavelength range of 0.35-2.5 µm were used to map spectral reflectance characteristics with the expert Tetracorder system (a modified absorption band-shaped comparison technique between obtained data and a library reference spectrum, Clark et al. 2003, 2023). The AVIRIS raw data were calibrated to radiance, ratioed to the solar spectrum and the atmospheric scattering and absorptions were removed to derive apparent surface reflectance (Thompson et al. 2019 and or Brodrick et al. 2021). The AVIRIS reflectance image cubes were mapped with tetracorder, which analyzed the spectra for hundreds of minerals, mineral mixtures, coatings, vegetation, man-made materials and other compounds. Tetracorder analyses different spectral regions for different compounds. While some minerals have unique spectral features (e.g., hematite, pyroxene), others have broadly-overlapping absorption features and only categories can be determined, e.g., Fe^{2+} bearing mineral.

3. Results and discussion

3.1 Particle size distribution

3.1.1 Particle size distribution in the Jökulsá á Fjöllum basin
The PSD of the sediments collected were analysed and the obtained minimally dispersed particle size distributions (MDPSD, i.e., near-natural aggregation state) and fully dispersed particle size distributions (FDPSD, i.e., aggregates completely dispersed) were compared to evaluate the state of particle aggregation in dust-emitting sediments. Jokulsá á Fjöllum basin includes Dyngjusandur (approximately 14 to 18 km away from the Vatnajökull glacier, see in detail in 3.1.2).

Both the MDPSD and FDPSD of the three types of sediments (top surface, fluvial and aeolian ripples) are characterised by left-skewed log-normal PSDs. PSDs of top sediment, fluvial sediments and aeolian ripples differ considerably, with an increasingly coarser PSD (Figure 3). The mean of the median diameters (mean median) from the FDPSDs of all samples types collected in the Jökulsá á Fjöllum basin was 133±174 µm [6.8,738, minimum and maximum], while that of MDPSDs reached 107±129 µm [6.4,502], indicating the variability of particle sizes. FDPSDs of top sediments had a much finer mean median diameter (31±15 µm) compared to the other type of samples: 102±91 and 354±203 µm for

372   fluvial sediments and aeolian ripples, respectively (Table 1). Similar results, in absolute and relative
373   values, were obtained for MDPSDs for all types of samples (Table 1).

374   The mean median diameter along the basin (from the glacier to the sea) of top sediments clearly
375   decreases, from 76 µm for FDPSD and 52 µm for MDPSD close to the moraine, down to 12 µm for
376   FDPSD and 11 µm for MDPSD just before the Holuhraun lava field (Figure 4) due to size segregation
377   during ponding and sedimentation of high sediment load water at Dyngjusandur. After the Holuhraun
378   lava field the mean median diameter of the top sediments increases again to up to 47 µm for FDPSD
379   and 41 µm for MDPSD, due to sediment input from tributary channels of the Jökulsá river, and then
380   decreases again, down to 29 µm for FDPSD and 27 µm for MDPSD, near the sea (Figure 4). For fluvial
381   sediments and ripples there are not enough samples, and the decreasing trend was not observed.

382   The analyses show similar results for MDPSD and FDPSD for samples with relatively finer mean median
383   diameters. However, and unexpectedly, MDPSD were finer than FDPSD samples for coarser mean
384   diameters. It is hypothesised that this might be due to the presence of pumice low-density particles,
385   fragile and easy to break into smaller light particles, which float in water, and therefore not detected
386   by the laser diffractometer in the case of the FDPSD, while the dry method used for obtaining the
387   MDPSD does not segregate pumice particles.

388   The mean diameter of the top sediments is reduced along the path from the glacier to the lava field.
389   This reduction occurs due to several factors. On the one hand, there is particle size segregation driven
390   by fluvial transport that carries sediment from the moraine to more distant areas. On the other hand,
391   vertical micro-segregation occurs during deposition at the ephemeral lake formed by the Holuhraun
392   lava field, which effectively acts as a natural dam. Because of this dam-like effect, sediment-laden
393   waters are temporarily impounded. Finer-grained top sediments gradually accumulate on top of the
394   coarser sediment layer deposited during the initial stage of the flooding-ponding-drying cycle. These
395   episodic events typically occur at intervals ranging from one to several days during the summer
396   season.

397   The water accumulated in this natural dam gradually permeates through the rocks and sediments and
398   subsequently flows through the Holuhraun lava field. These processes lead to sediment removal from
399   the water. This filtered water continues its course until it connects with tributary channels and the
400   segment of the Jökulsá á Fjöllum river that encircles the lava field. At this juncture, these sediment-
401   laden channels merge with clearer waters originating from the lava field post-filtration. Moreover,
402   beyond the lava field, the channels are typically incised, and flooding events are infrequent.
403   Consequently, the prevalence of fine-grained top sediments along this stretch, on the way to the sea,
404   is rare. This reduction in fine sediment cover significantly diminishes the potential for dust emissions.
405   Once the water reaches the sea, sediment deposition leads to extensive mudflats adorned with top
406   sediments, where emission becomes more likely once again if conditions are favourable.

407   3.1.2 Particle size distribution at different Icelandic dust hotspots
408   The median FDPSDs of top sediments found in most Iceland's dust-emitting regions (Dyngjusandur,
409   Skaftarsandur, Landeyjarsandur and Mælifellsandur) closely resemble the MDPSDs (Figure 5). This
410   underscores the limited degree of particle aggregation in these areas. However, in the cases of
411   Dyngjuvatn, Mýrdalssandur and Hagavatn the FDPSDs and MDPSDs of top sediments differ slightly
412   (Figure 5).

413

414 The mean median diameter of both the FDPSD and MDPSD for the 23 top sediments sampled across
415 Iceland is 56±69 µm [2.9,263, min., max.] and 55±62 µm [3.3,234], respectively. Notably, top
416 sediments from Mýrdalssandur and Dyngjuvatn exhibit coarser mean median diameters, measuring
417 147±108 and 146±156 µm for FDPSD, and 163±92 and 100±105 µm for MDPSD, respectively. These
418 diameters are more than two times coarser than the overall Iceland mean median diameter (Table 2).
419 Conversely, Skaftarsandur, Mælifellssandur and Landeyjarsandur show mean median diameters that
420 are similar those of the average top sediments in Iceland (Table 2). On the other hand, the top
421 sediments from Dyngjusandur and Hagavatn (the largest dust hotspots associated with ephemeral
422 lakes) exhibit the finest mean median diameters, specifically 24±15 and 16±12 µm for FDPSD, and
423 24±1 and 26±26 µm for MDPSD, respectively. These diameters are approximately two times finer than
424 the average of top sediments in Iceland (Table 2).

425 Our results show a general lack of cohesion in the dust-emitting top sediments of Iceland sources, as
426 evidenced by the similar FDPSD and MDPSD results. As discussed in Section 4 and 5, this strongly
427 suggests that in addition to saltation, aerodynamic entrainment of dust without saltation as an
428 intermediate process is likely a complementary dust emission process in Iceland due to reduced
429 cohesive forces.

430 **3.2 Mineralogy**

431   3.2.1 Mineralogy at Jökulsá á Fjöllum basin
432 Different sediments and locations of the Jokulsá á Fjöllum basin were analysed to describe the
433 variability in the region and therefore explain probable mineralogic fingerprints important for dust
434 emission models. The results show that amorphous phase is the prevailing component of the samples
435 analysed (79±11 %wt), being most probably volcanic glass and it's nano sized weathering product
436 (hydrated amorphous Si-bearing). Also showed anorthite (11±6.6 %, a Ca-plagioclase, $[Ca_{0.95-1}Na_{0.05-0}]Al_2Si_2O_8$),
437 augite (7.7±5.4 %, a pyroxene, $[Ca_xMg_yFe_z][Mg_{y1}Fe_{z1}]Si_2O_6$), andesine (1.7±5.9 %, a
438 plagioclase, $[Na_{0.5-0.7}Ca_{0.5-0.3}]Al_2Si_2O_8$), analcime (0.19±0.36 %, a Na-zeolite probably formed from the
439 devitrification of volcanic glass during weathering, $Na[AlSi_2O_6]·H_2O$), magnetite (<0.5 %, Fe_2O_4) and Ca-
440 mordenite (<0.1 %, a Ca-zeolite, $Ca_4[Al_8Si_40]O_{96}·28H_2O$) (Figure 6, Table S2).

441 The average composition of the top sediment samples comprises approximately 75±12 % volcanic
442 glass, 11±7.4 % anorthite, 9.9±6.4 % augite, 3.6±8.1 % andesine, along with trace amounts of
443 0.26±0.40 % analcime, 0.16±0.34 % Ca-mordenite, and <0.5 % magnetite. Fluvial sediments and
444 aeolian ripples have similar (or slightly higher) content of volcanic glass (80±12 and 86±4.7 %,
445 respectively), augite (6.6±4.0 and 4.8±1.7 %), and magnetite (<0.5 and <0.5 %). Anorthite is enriched
446 in fluvial sediments and aeolian ripples compared to top sediments (13±7.7 and 9.6±2.9 %,
447 respectively) and also analcime for the underlying fluvial sediments (0.23±0.43 %), with andesine and
448 Ca-mordenite contents being below the XRD detection limits in both the underlying fluvial sediments
449 and aeolian ripples (Figure 6, Table S2). The slight enrichment of fluvial sediments and aeolian ripples
450 in volcanic glass and the slight depletion in augite is likely due to the coarser particle size and the
451 prevalence of relatively large particles of high glass basalt with fine inclusions of crystalline minerals.
452 As these coarser particles break down into finer particles the occurrence of particles made of the
453 crystalline inclusions might increase. Thus, the finer top sediments might be slightly enriched in these

454   crystalline fine minerals (and slightly depleted in glass) in comparison to the coarser underlying fluvial
455   sediments and aeolian ripples.

456   The mineral composition of fluvial sediments is very homogeneous across the Jökulsá á Fjöllum basin;
457   however slight differences were observed for top sediment samples before and after the natural dam
458   of the Holuhraun lava field (Figure S2, Table S2). Before the natural dam, top sediments are enriched
459   in volcanic glass relative to those between the Holuhraun lava field and the sea (82 ± 2.2 and 60 ± 9.5 %,
460   respectively). Furthermore, after the Holuhraun field, andesine, traces of Ca-mordenite and hematite
461   are detected (11 ± 11, 0.48 ± 0.46, and <0.5 %, respectively). For fluvial sediments we observe similar
462   trends with volcanic glass enrichment before the Holuhraun lava field (85 ± 2.9 and 51 ± 18 %) and
463   minerals as andesine (16 ± 18 %), forsterite (Mg_2SiO_4) (2.8 %, 1 sample) and analcime (0.25 %, 1 sample)
464   being detected only after the Holuhraun lava field (Table S2). No trends were found for ripples due to
465   a lack of samples after the Holuhraun lava field. These differences are probably due to the different
466   source areas for pre- and post- Holuhraun lava field samples.

467   Reflectance spectra of aeolian ripples (Figure 7a) have broad electronic transitions due to Fe^{2+} with a
468   minimum at ~1.05 μm. Most spectra also have an inflection indicating a second electronic transition
469   of Fe^{2+} at ~2 μm (e.g., Burns, 1993). These spectra also have vibrational absorption features, with
470   combination bands of H_2O at 1.91 μm and Si-OH and/or Al-OH at 2.2 μm (e.g., Clark et al., 1990).
471   Overall, spectra are consistent with volcanic glass (Bell et al., 1976; Horgan et al., 2014) with possible
472   minor contributions of pyroxene (e.g., Cloutis and Gaffey, 1993) and weak hydration, likely mostly
473   from a hydrated amorphous silica product such as hydrated basaltic glass, allophane, imogolite, or
474   opal (e.g., Anderson and Wickersheim, 1964; Goryniuk et al., 2004; Rampe et al., 2012).

475   Spectra of top sediments are more variable (Figure 7b). All have broad Fe^{2+} electronic transitions
476   centred at 1.00-1.05 μm likely due to volcanic glass and pyroxene, as in the aeolian ripples. Most lack
477   an electronic transition near 2.0 μm, although one sample from a floodplain appears to have a weak
478   feature. All spectra have H_2O combinations at 1.91 μm, and most have OH overtones at 1.41-1.44 μm
479   (e.g., Clark et al., 1990). Other than from a few places on the moraine, all top sediments spectra also
480   have narrower features at 2.20-2.22 μm, which are combination bands of Si-OH and/or Al-OH (e.g.,
481   Clark et a., 1990). One spectrum (#21) also has a weaker Fe(III)-OH combination band at 2.29 μm, seen
482   in hydroxylated Fe-bearing minerals such as Fe smectite clay or ferrihydrite (e.g., Bishop et al., 2008).
483   Spectra from three sites on the moraine have broader, deeper 1.4 and 1.9 μm features, indicating that
484   the soil was wetter.

485   AVIRIS imaging spectroscopy data from the glacier to Holuhraun lava field, show the presence of water
486   in the sediments (absorption features between 1 to 1.5 μm), with clinopyroxene presence (absorption
487   features at 2-micron band), olivine, and Fe^{2+} bearing minerals, some of which may be Fe^{2+} in the
488   volcanic glass. These results are aligned with mineralogy from XRD and in-situ reflectance spectra
489   (Figure 8). In the main study areas, at AVIRIS scale, there are only trace to small local outcrops of
490   minerals as hematite, goethite, calcite, dolomite, chlorite/serpentine, gypsum, illite, muscovite,
491   montmorillonite, and vermiculite (Green et al., 2020). Some trace calcite is seen in Figure 8 and local
492   outcrops of chlorite/serpentine. The strong signatures of Fe^{2+} bearing minerals in the dark soils and
493   rocks make it difficult to detect hematite and goethite unless the concentration is high enough for the
494   Fe^{3+} absorptions to be stronger than Fe^{2+} absorptions.

3.2.2 Mineralogy of sediments from different Icelandic dust-emitting hotspots

The average composition of the top sediments from the Iceland's dust-emitting hotspots is also dominated by volcanic glass (68±26 % wt), followed by anorthite, augite and andesine (15±11 and 8.6±9.0 and 7.4±19 %), Fe-diopside (1.4±3.4 %, a pyroxene with a >50 % $MgSiO_3$ and 45-50 % $CaSiO_3$ composition), and traces of quartz (0.21±0.47 %), forsterite (0.61±1.7 %), wairakite (0.19±0.92 %), analcime (0.11±0.28 %), Ca-mordenite (<0.1 %), magnetite and hematite (<0.5 and <0.5 %) and pyrite (FeS_2 <0.5 %) (Figure 9, Table S3).

Volcanic glass content is higher at Dyngjuvatn, where top sediments are enriched in pumice, with a contribution of 89±3.8 %, followed by 82±2.3 % at Dyngjusandur, 81±2.8 % at Mælifellsandur, 75±8.9 % at Mýrdalssandur, 68 % (1 sample) at Skaftarsandur and 38±3.9 % at Landeyjarsandur (Figure 9, Table S3). At Hagavatn, however, the glass content reached only 13±14 %, with the mineralogy being dominated by andesine (53±11 %) and augite (29±3.8 %), with minor proportions of forsterite (4.7±1.3 %), hematite (<0.5 %) and magnetite (<0.5 %) (Figure 9, Table S3). Thus, in this case, the very high content of crystalline phases indicates a sediment originating from a slowly cooled lava allowing a widespread crystallisation of minerals from the melt.

A very similar mineral composition was found among top sediments from Mælifellsandur, Dyngjusandur, Skaftarsandur and Mýrdalssandur, where the main content was volcanic glass with some plagioclase and pyroxene species (Figure 9, Table S3). The highest content of volcanic glass was found at Dyngjuvatn and the lowest content at Hagavatn. The occurrence of magnetite was higher at Landeyjarsandur, Mælifellsandur and Mýrdalssandur, than in other dust-emitting hotspots, according to XRD analysis. As seen in section (3.1.2), Hagavatn and Dyngjusandur's top sediments have the smallest particle size, coinciding with the lowest volcanic glass content, in the first case, but quite high in the second. Meanwhile Dyngjuvatn's (pumice-rich) top sediments have the coarser particle size and the highest volcanic glass content. Mælifellsandur's and Mýrdalssandur's top sediments have similar mineral composition, but those of Mýrdalssandur are coarser (near the river mouth) in particle size compared to Mælifellsandur (upstream near the glacier). Landeyjarsandur's top sediments are similar in particle size to the ones from Mælifellsandur, but with half of the volcanic glass, and therefore with more plagioclase and pyroxene.

Compared to Baldo et al. (2020), who analysed PM_{10} mineralogy sampled in laboratory resuspension of Icelandic sediments, samples for the current study are very similar for Hagavatn, Mælifellsandur and Dyngjusandur, meanwhile for Landeyjarsandur and Mýrdalssandur the present results are lower for volcanic glass and so, higher for pyroxene and plagioclase. Baratoux et al. (2011) found a similar mineral composition of sediments from eolian ripples at Dyngjusandur, with predominance of volcanic glass (80-90 %). Moroni et al. (2018) found that the mineral composition of glaciofluvial sediments was dominantly volcanic glass in Dyngjusandur, Mýrdalssandur and Mælifellsandur, with lower proportions of plagioclase and pyroxene.

3.3 Mode of occurrence of Fe

3.3.1 Mode of occurrence of Fe at Jökulsá á Fjöllum basin

Iron speciation in dust-emitting sediments and surfaces control the amount of iron in the emitted dust and therefore the effect in ocean and terrestrial ecosystems and climate. The average of FeT content

535   in the dust emitting sediments of the Jokulsá á Fjöllum basin is 9.5±0.40 %wt (Table S4). Top sediments
536   as well as underlying fluvial sediments and eolian ripples exhibit similar average FeT contents with
537   values of 9.5±0.39 %, 9.5±0.43 %, and 9.4±0.41 %, respectively (Figure 10, Table S4). FeS, which
538   represents structural Fe found in volcanic glass and certain Fe-bearing crystalline species, constitutes
539   for the majority of FeT content, accounting for 80±6.3 %. This is, followed by smaller proportions of
540   FeM (magnetite) at 16±5.5 %, FeD (hematite/goethite) at 2.6±1.6 %, and FeA (readily exchangeable
541   Fe) at 1.2±0.40 % (Figure 10, Table S4). It is worth noting that these proportions are quite consistent
542   across top sediments, fluvial sediments and eolian ripples, with FeS, FeM, FeD and FeA percentages
543   of 79±6.5 %, 16±5.4 %, 3.5±1.5 % and 1.3±0.39 % in the top sediments. In fluvial sediments, these
544   values are 82±8.7 %, 15±7.8 %, 2.2±1.4 % and 1.2±0.44 % and in eolian ripples, they are 80±2.4 %,
545   18±2.4 %, 1.2±0.41 % and 0.85±0.22 % respectively (Figure 10, Table S4). Notably, there is a difference
546   in magnetite proportions between fluvial sediments from the pre-Holuhraun lava field and those from
547   the post-Holuhraun, with FeM accounting for 19±4.5 % and 11±1.3 % of total Fe, respectively. This
548   variation results in a reverse scenario for FeS, with percentages of 77±6.4 % and 84±1.9 %, respectively
549   (Figure 10, Table S4).

550   3.3.2 Mode of occurrence of Fe at different Icelandic dust-emitting hotspots
551   The content of FeT and proportions of FeS, FeA, FeD and FeM in sediments from Iceland's dust-
552   emitting hotspots are summarised in Table S5 and Figure 11.

553   The average FeT content in Iceland's top sediments is 9.3±1.5 %, with the highest concentrations
554   observed in Mælifellsandur and Mýrdalsandur, ranging from 10.0 % to 11.6 % wt, while the lowest are
555   found at Hagavatn and Dyngjuvatn, ranging from 5.5 % to 9.1 % wt. On average, FeS accountsfor
556   79±5.4 % of the FeT, with minimum proportions of 65 % in one sample from Dyngjusandur and a
557   maximum of 89 % in one from Mælifellsandur. However, most samples are in the range of 75-80 %.

558   FeM constitutes 15±4.6 % of FeT, with minimum proportions of 7.2 % in one sample from
559   Landeyjarsandur and a maximum of 25 % in one from Dyngjusandur, but most samples fall within the
560   10-20 % range, with the highest proportions typically exceeding 20 % in Dyngjusandur. FeD accounts
561   for 5.0±3.1 % of FeT, with minimum proportions of 1.4 % in one sample from Dyngjusandur and a
562   maximum of 12 % in one from Hagavatn, but most samples fall within the 2-9 % range. FeA represents
563   only 1.6±0.74 % of FeT, with minimum proportions of 0.75 % in one sample from Dyngjusandur and a
564   maximum of 3.4 % in one from Hagavatn, but the majority of samples fall within the 1-2 % range.

565   The absolute contents of magnetite and hematite/goethite are quite low in the samples, making XRD
566   quantitative analysis uncertain. Consequently, the correlation with FeM and FeD is weak. This
567   highlights the importance of employing the chemical sequential extraction (Shi et al. 2009) to assess
568   the mode of occurrence of Fe and further constrain the mineral content of iron oxides. As mentioned
569   in previous sections (3.1.2 and 3.2.2), Dyngjusandur and Hagavatn have similar mean median particle
570   size, but different volcanic glass content. The content of FeS is similar between them, but in the other
571   hand, Hagavatn has higher proportions of FeA and FeD than FeM and Dyngjusandur more proportion
572   of FeM than FeA and FeD. Nevertheless, no correlation was found between mineralogy (from XRD)
573   and Fe speciation.

574

3.4 Spectroscopic indicators of mineral sorting

Spectra acquired in situ of top sediments and ripples show systematic variations with distance from their source (Figure 12). Aeolian ripples, composed of ~100 µm-sized grains weathered out of recent lava flows, were generally measured on or near the lavas from which they are sourced and are coarser grained than top sediments. Thus, their spectra are dominated by primary volcanic phases, including volcanic glass and pyroxene, with minor alteration, either by magmatic fluids (hydrating the volcanic glass) or later alteration. Their spectra are dark (low albedo), have weaker H_2O combination bands at 1.91 µm, and stronger Fe^{2+} electronic transitions near 1 and 2 µm than most top sediments. Interestingly, the depth of the absorption feature around 2.21 µm is slightly stronger in these samples and most likely is from a hydrated amorphous silica phase (Figure 12c). These samples unsurprisingly show no systematic trends with distance from the glacier.

Top sediments, on the other hand, show stronger trends with distance from the glacier (Figure 12). The albedo, measured as the mean from 1.62-1.63 µm is brighter with increasing distance (Figure 12d). This may be due to a change in mineralogy from primary volcanic glass, olivine, and pyroxene to brighter alteration products, including zeolites and phyllosilicate minerals, or due to decreasing particle size, as volume scattering is enhanced with smaller grains. More likely, it is a combination of both factors. With the exception of locations on the moraine that were wetter at the surface, the depth of the absorption feature due to H_2O at 1.91 µm increases with distance from the glacier (Figure 12b). Conversely, the depth of the ≈1 µm Fe^{2+} electronic transition decreases (Figure 12a). These variations are most likely the result of mechanical sorting, with finer grained hydrated, altered phases becoming dominant downstream relative to coarser, unaltered volcanic glass.

The loss of volcanic glass and potentially amorphous hydrated silica within top sediments is also supported by closer examination of the spectra. In spectra of some top sediments, the ≈1.0 µm Fe^{2+} electronic transition minimum shifts to slightly shorter wavelengths (≈1.03 µm in top sediments vs 1.05 µm in ripples), and a secondary electronic feature at ≈1.2 µm is typically weaker or absent. These shifts are consistent with the proportion of pyroxene to volcanic glass increasing (Horgan et al., 2014). In addition, the ≈2.2 µm combination feature shifts from 2.22-2.25 µm in the ripples to 2.21 µm in some top sediment samples. The longer wavelength minima and broader features are more typical of hydrated amorphous silica (e.g., opal), whereas the shorter wavelength minima suggest the presence of a more ordered phase with Al-OH bonds.

4. Contrasts in composition, particle size distribution, aggregation/cohesion and reflectance spectra between Icelandic hotspots and a typical hot desert dust hotspot

Our findings reveal significant between sediments from the Moroccan Sahara (as described in Gonzalez-Romero et al., 2023) and those collected and analysed in Iceland. It is important to note that the Moroccan samples used for comparison were obtained from the Lower Drâa Valley, an arid inland drainage basin and a prominent dust hotspot, which is broadly representative of numerous crustal dust source areas in hot desert environments.

The differences in sediment composition are closely intertwined with the particle size distribution and aggregation/cohesion characteristics of these sediments. For instance, when we examine the mean

614   median diameters of the FDPSD and MDPSD for top sediments collected from the lowlands and the
615   ephemeral lakes of Iceland (Dyngjusandur), we observe a relatively close similarity in sizes (31 and 32
616   μm, respectively) (as detailed in Table 3). In contrast, crusts from the lowlands in the Saharan source
617   exhibit markedly different mean median diameters (7 and 131 μm, as reported by González-Romero
618   et al., 2023) (Table 3). Therefore, the FDPSD mean diameters for just crusts in the lowlands of the
619   Saharan source are four times finer than those found in top sediments in Iceland. For the underlying
620   fluvial sediments, we found that the MDPSD median diameters are 1.5 times coarser in the Saharan
621   source in comparison to Iceland (115 and 74 μm, respectively). In contrast, for the FDPSD the mean
622   median diameter is finer in the Saharan source than in Iceland (22 and 102 μm, respectively).

623   The resemblance between the FDPSD and MDPSD of top sediments in Dyngjusandur, as well as the
624   significant disparity with those from the Sahara, are attributed to the varying levels of aggregation and
625   cohesion. These differences in aggregation are further substantiated by SEM observations (as shown
626   in Figure 13a and b). They are likely a consequence of the paucity of cementing minerals in the Iceland
627   top sediments, namely low levels of carbonate and sulphate content, as well as the absence of clay
628   minerals. These factors contribute to the prevalence of dispersed and non-cohesive sediments in
629   Iceland. The underlying fluvial sediments which consist mainly of coarse particles, primarily individual
630   granules derived from volcanic rock (as depicted in Figure 13c), also stands in contrast to the Sahara's
631   dust-emitting sediments, which often exhibit particle aggregation. Notably distinct were Iceland's
632   dust-emitting top sediments that showed a high enrichment of pumice, an exceedingly fragile and
633   low-density volcanic rock, as seen in the Dyngjuvatn samples. In these cases, the particles often
634   displayed elongated shapes and were accompanied by aggregation of finer particles (refer to Figure
635   13d, e, and f). This distinctive characteristic led to a measurement artifact that resulted in unusually
636   coarser FDPSD readings compared to MDPSD.

637   The lack of aggregation and cohesion of Icelandic dust-emitting sediments in comparison to the
638   Saharan source strongly suggests that saltation in Iceland should be efficient, while at the same time
639   dust could be emitted also by direct aerodynamic entrainment. Usually, dust emission due to
640   aerodynamic entrainment is much less efficient than that generated by saltation bombardment,
641   because interparticle cohesive forces, encompassing Van der Waals forces, electrodynamic forces, and
642   chemical forces (e.g., Castellanos, 2005), increase on average with decreasing particle size. This results
643   in an average minimum entrainment threshold for sand-size particles of around 70 - 100 μm (Shao
644   and Lu, 2000; Shao and Klose, 2016). Toward smaller and larger particle sizes, increasing cohesive and
645   gravitational forces, respectively, require stronger lifting forces for particle entrainment. However, if
646   cohesive forces are weaker than on average, as it is the case in Iceland, the entrainment threshold for
647   dust-size particles can be reduced to a value similar to or possibly even lower than for sand-size
648   particles, enabling efficient direct aerodynamic dust emission without saltation as an intermediate
649   process (Klose and Shao, 2013; Shao and Klose, 2016).

650   In contrast to Saharan dust-emitting sediments, which comprise quartz, feldspars, clays, calcite,
651   dolomite, hematite/goethite, and halite, sediments from Iceland's dust sources are predominantly
652   composed of amorphous volcanic glass. They also contain anorthite (Ca-plagioclase), augite
653   (pyroxene), and andesine (plagioclase), with smaller quantities of analcime, magnetite, Ca-modernite,
654   and hematite. These pronounced differences in composition have distinct implications for ice
655   nucleation, radiative forcing, and nutrient deposition. While the effects of the main minerals in hot

656   deserts on these processes are relatively well-understood, the impact of volcanic glass, which
657   constitutes the majority of Icelandic dust, remains largely unexplored and requires further research.
658   One notable difference is the average iron (FeT) content in Icelandic sediments, which is
659   approximately three times higher than that in Saharan sediments. Additionally, the proportion of FeS
660   in FeT is greater in Iceland than in the Sahara, comprising 79 % vs 67 % for top sediments, 82 % vs 68
661   % for underlying fluvial sediments, and 80 % vs 73 % for eolian ripples (as detailed in Table 4 and Figure
662   14). The proportion of Fe from hematite and goethite (FeD %) in Iceland is lower than in the Sahara
663   (1-7 % vs 31 %) while the proportion of FeM is higher in Iceland (9.5-18 % vs negligible) yielding to a
664   potentially different climate effect from the emitted dust (Table 4 and Figure 14). Furthermore, the
665   proportion of FeA, which is highly bioavailable, is lower in Iceland for top sediments (1.3 % vs. 1.9 %
666   of the FeT content), fluvial sediments (1.2 % vs. 1.4 %), and eolian ripples (0.85 % vs. 1.0 %) (as shown
667   in Table 4 and Figure 14). It is important to note that, even though the % FeA in Icelandic sediments is
668   slightly lower, the amount of bioavailable Fe per mass in Iceland's dust-emitting sediments is higher
669   than that of Saharan sediments due to the higher FeT contents in Icelandic samples. Similar
670   mineralogical content was found by Baldo et al. (2020), with a major proportion of volcanic glass in
671   the sediments, followed by anorthite and augite at Dyngjuvatn and Hagavatn. Fe proportions and total
672   amount are also very similar to those obtained by Baldo et al. (2020).

673   Spectra of dust source sediments from Morocco are markedly different than those from Iceland as
674   seen also in the mineralogy (Figure 7a, b, and c). Spectra from Morocco have electronic transitions
675   and charge transfers of Fe^{3+} at wavelengths <1 µm, related to hematite and goethite presence (Figure
676   7a, b, and c), whereas spectra from Iceland have broader Fe^{2+} electronic transitions at wavelengths >1
677   µm and sometimes near 2 µm, related to the volcanic glass and pyroxene proportion (Figure 7c). At
678   longer wavelengths, spectra of sediments from Morocco show features of phyllosilicates, including
679   illites and smectites, whereas in Iceland this is not observed, except the 2.2 micron feature in Figure 7
680   may be due to hydrated silica plus phyllosilicates such as montmorillonite.

681   **5. A conceptual model for dust emission, particle size and mineralogy for Dyngjusandur, a**
682   **major Iceland dust hotspot**

683   Dust-emission in Iceland is primarily governed by glaciofluvial environments. These regions are
684   characterized by the melting of glaciers that have accumulated substantial volcanic sediments and ash
685   over geological time. Subsequently, the fluvial erosion of these sediments transports significant
686   quantities of fine materials, which are deposited in extensive, flat areas during floods (Figure 15). This
687   phenomenon is particularly prevalent in the Jokulsá á Fjöllum basin and other similar locations like
688   Dyngjuvatn, Mælifellssandur, and Mýrdalssandur, with heightened activity during the summer months
689   when glacial melting accelerates. Once these deposited fine sediments dry out, they become prone to
690   dust emission when appropriate wind patterns prevail. In the Jökulsá á Fjöllum basin, this scenario is
691   specially favoured, with a glacial river flowing from the Vatnajökull moraine to Holuhraun, where a
692   recent volcanic eruption (July 29, 2014 to February 27, 2015 with an 85 km² of surface, Geiger et al.,
693   2016) generated a natural dam, and some of the fluvial channels arising from the moraine transport
694   large volumes of sediments across a flat and extensive region (Figure 15). In this endorheic flat,
695   continuous summer floods lead to cyclic sediment deposition. Coarser fluvial sediments are deposited
696   first and are subsequently covered by top sediments of very fine grains formed after each cycle
697   through the deposition of suspended fine particles following drying or infiltration of ponded waters

698   (Figure 16). Following sediment deposition, waters infiltrate and traverse the lava field, flowing to the
699   other side of the natural dam with minimal sediment load. On the other side of the dam, these pristine
700   waters join those from the other channels unaffected by the dam and flow toward the sea. Because
701   the dam stops part of the floods and because the river is more incised, overflows and sediment flats
702   alongside the river are very reduced from the dam to the sea. However, large flooding flats at the sea
703   once again contain sediments prone to dust emission. Such sedimentation, particle size fractionation,
704   drying and dust emission processes are generally repeated daily under favourable conditions in
705   summer. The aeolian ripples are formed in the dry part of the cycle and can be mobilised by the wind
706   and trigger the emission of dust by saltation. However, the lack of cohesive forces in the sediments
707   may also allow direct aerodynamic entrainment of dust at lower wind speeds without the need of
708   saltation (Figure 16).

6. Conclusions

709

710   This study has undertaken a comprehensive examination of dust-emitting sediments in Iceland,
711   focusing on their particle size distributions, mineralogy, and Fe mode of occurrence. Our findings
712   reveal distinctive characteristics among various sites, with Hagavatn and Dyngjusandur exhibiting the
713   finest particle size distributions, and Mýrdalssandur and Dyngjuvatn showing the coarsest. Despite
714   these variations, the overall particle size distributions in Iceland's top sediments, whether fully or
715   minimally dispersed, exhibit remarkable similarities. Notably, these distributions sharply contrast with
716   those observed in a dust hotspot in the Moroccan Sahara. Iceland's top sediments are approximately
717   four times coarser than fully dispersed Moroccan crusts, yet, these fully dispersed Iceland top
718   sediments are finer than the minerally dispersed Moroccan crusts, prevalent in the Moroccan Sahara.
719   These distinctions underscore the relatively limited interparticle cohesion in Iceland, a characteristic
720   that sets it apart. The scarcity of cohesion implies an efficient saltation bombardment process, and at
721   the same time suggests the possibility of direct aerodynamic entrainment of dust in this region. This
722   contrasts with the cohesive sediments typically found in hot desert environments, where interparticle
723   cohesion hinders dust aerodynamic entrainment, making saltation the primary mechanism for dust
724   emission.

725   Iceland's dust-emitting sediments primarily consist of black volcanic glass, constituting a substantial
726   proportion ranging from 70% to 85% by weight. Plagioclase and pyroxenes contribute 10% to 15% and
727   4% to 8%, respectively, with traces of zeolites and Fe-oxides present. Consistent compositional
728   patterns emerge across most dust-emitting regions in Iceland, except for Landeyjarsandur and
729   Hagavatn. In these regions, sediments display diminished glass content (35% and <0.1%, respectively)
730   and heightened levels of plagioclase and pyroxenes, reaching up to 65% and 31%, respectively. These
731   compositional variations are starkly distinct from Saharan dust-emitting sediments, owing to the
732   differing volcanic and sedimentary origins of the respective dust sources. Notably, in Saharan
733   sediments, the presence of salts, carbonates, and clays promotes the formation of aggregates that
734   increase particle size and sediment cohesion. The composition of Fe-oxides also varies between the
735   two regions, with hematite and goethite being predominant in the Sahara, while Iceland's sediments
736   predominantly contain magnetite. The specific role of black volcanic glass in dust-radiation and dust-
737   cloud interactions remains inadequately described, contributing to a limited understanding of its
738   impact on climate. Further research is essential to unravel the complexities of these interactions and
739   their implications for climate.

740   The distribution of Fe in the top sediments of Jökulsá á Fjöllum, as well as in the underlying fluvial
741   sediments and the aeolian ripples, exhibits homogeneity in its mode of occurrence. The averaged bulk
742   Fe content (FeT) is 9.5±0.40 %wt, with structural Fe (FeS) constituting 80±6.3%, and Fe in magnetite
743   (FeM) accounting for 16±5.5%. Minor variations are observed in the proportions of Fe as
744   hematite/goethite (FeD) and readily exchangeable- and nano-Fe (FeA). Notably, the top sediments
745   display a significant presence of readily exchangeable Fe and hematite/goethite, attributed to
746   heightened glass weathering in the fine top sediment compared to coarser underlying layers and
747   aeolian ripples. Similar trends were identified in various Icelandic sources, with Mælifellsandur and
748   Mýrdalssandur exhibiting higher mean FeT (11±0.48% and 11±0.41%, respectively). Hagavatn and
749   Skaftarsandur showed a maximum proportion of FeA (2.7±1.0%) and (2.6%, 1 sample), respectively.
750   Landeyjarsandur displayed the maximum FeD proportion (7.2±2.1%), while Dyngjusandur exhibited
751   the highest proportion of FeM (18±4.6%). In comparison to the Moroccan Saharan, although
752   proportions are similar, the bulk Fe content in Iceland is threefold higher. Consequently, for the same
753   emitted dust mass, the absolute mass of FeA is three times greater, with FeD being smaller, and FeM
754   emerging as the major contributor, resulting in a potentially distinct impact on oceans and terrestrial
755   ecosystems and yielding diverse implications for climate.

756   Airborne and in-situ spectroscopy results are broadly consistent with XRD and size results. The spectra
757   of ripples are dark (low albedo) and dominated by primary volcanic phases and show no systematic
758   trends with distance from the glacier. Top sediments show trends with distance from the glacier
759   (Figure 12), with the albedo being brighter with increasing distance partly due to decreasing particle
760   size, which most likely is the result of mechanical sorting, with finer grained hydrated, altered phases
761   becoming more prevalent downstream relative to coarser, unaltered volcanic glass. There is lack of
762   significant clay minerals, carbonates and salts (even though, traces of carbonates and serpentines
763   have been found with Tetracorder). The marked differences in composition between Icelandic and
764   Moroccan sources are also captured. Spectra from Morocco have electronic transitions and charge
765   transfers of Fe^{3+} at wavelengths <1 µm, related to hematite and goethite, while spectra from Iceland
766   have broader Fe^{2+} electronic transitions at longerwavelengths, related to the volcanic glass and
767   pyroxene.

768   A conceptual model has been formulated to elucidate the elevated dust emissions observed in
769   Dyngjusandur, Iceland. This model encompasses several key factors contributing to the phenomenon.
770   Firstly, the historical entrapment of substantial amounts of volcanic sediments and ash by the glacier
771   has established a reservoir of materials awaiting liberation. The accelerated melting of the glacier,
772   particularly intensified during summer and influenced by underlying volcanism, releases significant
773   volumes of fresh sediment. Notably, a volcanic field active in 2014-2015 functions as a natural dam,
774   triggering extensive floods that inundate large plains with sediments prone to inducing dust emissions.
775   These floods exhibit a daily recurrence under specific summer conditions, fostering sedimentation,
776   particle fractionation, drying, and cycles of dust emission. The inherent nature of the sediments,
777   characterized by black basalt detritus and volcanic ash with a predominant glassy composition, results
778   in minimal particle aggregation and cohesion. Moreover, the frequent and extensive vertical particle
779   size segregation during the flooding cycles contributes to the coverage of vast areas with very fine
780   sediments, thereby facilitating dust emission. The synergy of these geological, climatic, and
781   environmental factors provides a comprehensive understanding of the intricate processes driving high
782   dust emissions in Dyngjusandur.

Code availability. The code used in this paper is provided by Clark (2023, https://github.com/PSI-edu/spectroscopy-tetracorder).

Data availability. Data used in this paper are given in the main paper itself and in the Supplement. If **needed, data are also available upon request by emailing the authors.**

Author contributions. CPG-P proposed and designed the field campaign with contributions of AA, KK, MK and XQ. The Campaign was implemented by CPG-P, AA, CGF, AGR, KK, MK, AP, XQ and JYD. The samples were collected by CPG-P, AA, AGR, MK, AK, RG and XQ and analysed by AGR, PC and NM. Spectroscopy was analysed by AK, RG, BLE, PB and RNC. AGR performed the visualization and writing of the original draft manuscript and CPG-P and XQ supervised the work. CPG-P and XQ re-edited the manuscript and all authors contributed in data discussion, reviewing and manuscript finalization.

Competing interests. At least one of the (co-)authors is a member of the editorial board of Atmospheric chemistry and Physics.

Acknowledgements

The field campaign and its associated research, including this work, was funded by the European Research Council under the Horizon 2020 research and innovation programme through the ERC Consolidator Grant FRAGMENT (grant agreement No. 773051) and the AXA Research Fund through the AXA Chair on Sand and Dust Storms at BSC. CGF was supported by a PhD fellowship from the Agència de Gestió d'Ajuts Universitaris i de Recerca (AGAUR) grant 2020_FI B 00678. KK was funded by the Deutsche Forschungsgemeinschaft (DFG, German Research Foundation) – 264907654; 416816480. MK has received funding through the Helmholtz Association's Initiative and Networking Fund (grant agreement no. VH-NG-1533). We acknowledge the EMIT project, which is supported by the NASA Earth Venture Instrument program, under the Earth Science Division of the Science Mission Directorate. We thank Dr. Eva L. Scheller for the help during the field spectroscopy measurements. We thank Dr. Pavla Dagsson Waldhauserova from the Agricultural university of Iceland for the invaluable support and help during the field campaign. We thank Thomas Dirsch for the uncontauble driving hours and mechanical support during the soil sampling. We thank Paul Ginoux for providing high-resolution global dust source maps, which were very helpful for the identification of the FRAGMENT experimental sites. We thank the staff from the ranger station at Dreki as well as the wardens of the Dreki campsite and the Dreki mountain rescue service for their valuable support and advice. We also thank Vilhjalmur Vernharðsson and his crew from Fjalladýrð for their permanent logistic help. Without all of them, the measurement campaign would not have been successfully feasible.

7. References

Anderson J.H. and Wickersheim K.A.: Near Infrared Characterization of Water and Hydroxyl Groups on Silica Surfaces. Surface Science 2, 252–60, 1964. https://doi.org/10.1016/0039-6028(64)90064-0.

Arnalds Ó., Gisladottir F.O., Sigurjonsson H.: Sandy deserts of Iceland: an overview. Journal of Arid Environments, 47, 3, 359-371, 2001.

Arnalds Ó.: Dust sources and deposition of aeolian materials in Iceland. Icelandic agricultural sciences, 23, 3-21, 2010.

Arnalds Ó., Olafsson H. and Dagsson-Waldhauserova P.: Quantification of iron-rich volcanogenic dust emissions and deposition over the ocean from Icelandic dust sources, Biogeosciences, 11, 6623-6632. https://doi.org/10.5194/bg-11-6623-2014, 2014.

Arnalds Ó., Dagsson-Waldhauserova P., Olafsson H.: The Icelandic volcanic aeolian environment: Processes and impacts — A review. Aeolian Research, 20, 176-195, 2016.

Arnalds Ó., Dagsson-Waldhauserova P., Olafsson H.: Dyngjusandur: a rapidly evolving hyperactive dust source north of Vatnajökull glacier, Iceland. Geophysical Research Abstracts, 20, EGU2018-14764, 2018.

Baldo C., Formenti P., Nowak S., Chevaillier S., Cazaunau M., Pangui E., Di Baggio C., Doussin J.F., Ignatyev K., Dagsson-Waldhauserova P., Arnalds O., MacKenzie A.R., Shi Z.: Distinct chemical and mineralogical composition of Icelandic dust compared to Northern African and Asian dust. Atmospheric Chemistry and Physics, 20, 13521-13539, 2020.

Baldo C., Formenti P., Di Biagio C., Lu G., Song C., Cazaunau M., Pangui E., Doussin J.-F., Dagsson-Waldhauserova P., Arnalds O., Beddows D., MacKenzie A.R., Shi Z.: Complex refractive index and single scattering albedo of Icelandic dust in the shortwave spectrum, EGUsphere [preprint], https://doi.org/10.5194/egusphere-2023-276, 2023.

Baratoux D., Mangold N., Arnalds O., Bardintzeff J.M., Platevoët B., Grégoire M. and Pinet P.: Volcanic sands of Iceland - Diverse origins of aeolian sand deposits revealed at Dyngjusandurand Lambahraun. Earth Surf. Process. Landforms, Vol.36, 1789-1808, 2011.

Beckett F., Kylling A., Sigurðardóttir G., von Löwis S., Witham C.: Quantifying the mass loading of particles in an ash cloud remobilized from tephra deposits on Iceland, Atmos. Chem. Phys., 17, 4401–4418, https://doi.org/10.5194/acp-17-4401-2017, 2017.

Bell P.M., Mao H.K., and Weeks R.A.: Optical Spectra and Electron Paramagnetic Resonance of Lunar and Synthetic Glasses - A Study of the Effects of Controlled Atmosphere, Composition, and Temperature. Proc. Lunar Sci. Conf. 7, p. 2543–59, 1976.

Bishop J.L., Lane M.D., Dyar M.D., and Brown A.J.: Reflectance and Emission Spectroscopy Study of Four Groups of Phyllosilicates: Smectites, Kaolinite-Serpentines, Chlorites and Micas." Clay Minerals 43, 1, 35–54, 2008. https://doi.org/10.1180/claymin.2008.043.1.03.

Brodrick, P.G., Thompson, D.R., Fahlen, J.E., Eastwood, M.L., Sarture, C.M., Lundeen, S.R., Olson-Duvall, W., Carmon, N., Green, R.O.: Generalized radiative transfer emulation for imaging spectroscopy reflectance retrievals. Remote Sens. Environ. 261, 112476, 2021

Bullard J.E.: Contemporary glacigenic inputs to the dust cycle. Earth Surf. Proc. Land., 38, 71-89. https://doi.org/10.1002/esp.3315, 2013.

Bullard J.E., Baddock M., Bradwell T., Crusius J., Darlington E., Gaiero D., Gassó S., Gisladottir G., Hodgkins R., McCulloch R., McKenna-Neuman C., Mockord T., Stewart H., Thorsteinsson T.:

863   High-latitude dust in the Earth system. Reviews of Geophysics, 54, 447-485.
864   doi:10.1002/2016RG000518, 2016.
865 Burns R.G.: Mineralogical Applications of Crystal Field Theory. Cambridge University Press, 1993.
866 Castellanos A.: The Relationship Between Attractive Interparticle Forces and Bulk Behaviour in Dry and
867   Uncharged Fine Powders. Advances in Physics, 54, 4, 263-376, 2005.
868 Cheary R.W., Coelho A.: A fundamental parameters approach to X-ray line profile fitting. Journal of
869   Applied Crystallography 25, 109–121, 1992.
870 Claquin T., Schulz M., Balkanski Y.J.: Modeling the mineralogy of atmospheric dust sources. Journal
871   Geophysical Research. 104, D18, 22243-22256, 1999.
872 Clark R.N., and Roush T.L.: Reflectance Spectroscopy: Quantitative Analysis Techniques for Remote
873   Sensing Applications. Journal of Geophysical Research, 89, B7, 6329-6340, 1984.
874   https://doi.org/198410.1029/JB089iB07p06329.
875 Clark R.N., King T.V.V., Klejwa M., Swayze G.A., and Vergo N.: High Spectral Resolution Reflectance
876   Spectroscopy of Minerals. Journal of Geophysical Research 95, no. B8, 12653–80, 1990.
877   https://doi.org/199010.1029/JB095iB08p12653.
878 Clark R.N., Swayze G.A., Livo K.E., Kokaly R.F., Sutley S.J., Dalton J.B., McDougal R.R., Gent C.A.: Imaging
879   spectroscopy: Earth and planetary remote sensing with the USGS Tetracorder and expert
880   systems. The Journal of Geophysical Research, v.108, 2003. doi:10.1029/2002JE001847.
881 Clark, R. N., Swayze, G. A., Livo, K. E., Brodrick, P., Noe Dobrea, E., Vijayarangan, S., Green, R. O.,
882   Wettergreen, D., Garza, A. C., Hendrix, A., García-Pando, C. P., Pearson, N., Lane, M., González-
883   Romero, A., Querol, X. & the EMIT and TREX teams. Imaging spectroscopy: Earth and planetary
884   remote sensing with the PSI Tetracorder and expert systems: from Rovers to EMIT and
885   Beyond, Planetary Science J., in review, 2023.
886 Cloutis E.A., and Gaffey M.J.: Pyroxene Spectroscopy Revisited: Spectral-Compositional Correlations
887   and Relationship to Geothermometry. Journal of Geophysical Research 96, E5, 22,809-22,826,
888   1991. https://doi.org/199110.1029/91JE02512.
889 Cvetkovic B., Dagsson-Waldhauserova P., Petkovic S., Arnalds O., Madonna F., Proestakis E., Gkikas A.,
890   Vimic A.V., Pejanovic G., Rosoldi M., Ceburnis D., Amiridis V., Lisá L., Nickovic S., Nikolic J.: Fully
891   dynamic high-resolution model for dispersion of icelandic airborne mineral dust. Atmosphere,
892   13, 9, 1345. https://doi.org/10.3390/atmos13091345, 2022.
893 Dagsson-Waldhauserova P., Arnalds O., Olafsson H., Hladil J., Skala R., Navratil T., Chadimova L., and
894   Meinander O.: Snow–Dust Storm: Unique case study from Iceland, March 6–7, 2013. Aeolian
895   Research, 16, 69-74. https://doi.org/10.1016/j.aeolia.2014.11.001, 2015.
896 Dagsson-Waldhauserova P., Magnusdottir A.O., Olafsson H., Arnalds O.: The Spatial Variation of Dust
897   Particulate Matter Concentrations during Two Icelandic Dust Storms in 2015, 2016.
898 De la Torre A.G., Bruque S., Aranda M.A.G.: Rietveld quantitative amorphous content analysis. Journal
899   of Applied Crystallography, 34:196-202, 2001.
900 De Longueville F., Hountondji Y. C., Henry S., Ozer P.: What do we know about effects of desert dust
901   on air quality and human health in West Africa compared to other regions?. Sci. Total Environ.,
902   409, 1-8, 2010.
903 Di Biagio C., Formenti P., Balkanski Y., Caponi L., Cazaunau M., Pangui E., Journet E., Nowak S., Andreae
904   M.O., Kandler K., Saeed T., Piketh S., Seibert D., Williams E., Doussin J.F.: Complex refractive
905   indices and single-scattering albedo of global dust aerosols in the shortwave spectrum and
906   relationship to size and iron content. Atmos. Chem. Phys., 19, 15503-15531.
907   https://doi.org/10.5194/acp-19-15503-2019, 2019.

908 Dragosics M., Meinander O., Jónsdóttír T., Dürig T., De Leeuw G., Pálsson F., Dagsson-Waldhauserova
909   P., Thorsteinsson T.: Insulation effects of Icelandic dust and volcanic ash on snow and ice.
910   Arab. J. Geosci., 9, 126, https://doi.org/10.1007/s12517-015-2224-6, 2016.
911 Engelbrecht J.P., Moosmüller H., Pincock S., Jayanty R.K.M., Lersch T., Casuccio G.: Technical note:
912   Mineralogical, chemical, morphological, and optical interrelationships of mineral dust re-
913   suspensions. Atmos. Chem. Phys., 16, 10809-10830. https://doi.org/10.5194/acp-16-10809-
914   2016, 2016.
915 Einarsson M.A.: Climate of Iceland. Van. Loon (Ed.), World Survey of Climatology, 15, Chapter 7,
916   Elsevier, Amsterdam, 672-697. Atmosphere, 7(6), 77.
917   https://doi.org/10.3390/atmos7060077, 1984.
918 Formenti P., Caquineau S., Chevaillier S., Klaver A., Desboeufs K., Rajot J.L., Belin S., Briois V.:
919   Dominance of goethite over hematite in iron oxides of mineral dust from Western Africa:
920   Quantitative partitioning by X-ray absorption spectroscopy. J. Geophys. Res. Atmos., 119,
921   12740-12754. https://doi.org/10.1002/2014jd021668, 2014.
922 Geiger H., Mattson T., Deegan F.M., Troll V.R., Burchardt S., Gudmundsson Ó., Tryggvason A.,
923   Krumbholz M., Harris C.: Magma plumbing for the 2014–2015 Holuhraun eruption, Iceland.
924   Geochemistry, Geophysics, Geosystems, 17, 8, 2953-2968, 2016.
925 González-Flórez C., Klose M., Alastuey A., Dupont S., Escribano J., Etyemezian V., Gonzalez-Romero A.,
926   Huang Y., Kandler K., Nikolich G., Panta A., Querol X., Reche C., Yus-Díez J., Pérez García-Pando
927   C.: Insights into the size-resolved dust emission from field measurements in the Moroccan
928   Sahara, Atmos. Chem. Phys., 23, 7177–7212, https://doi.org/10.5194/acp-23-7177-2023,
929   2023.
930 González-Romero A., González-Florez C., Panta A., Yus-Díez J., Reche C., Córdoba P., Moreno N.,
931   Alastuey A., Kandler K., Klose M., Baldo C., Clark R.N., Shi Z.B., Querol X., Pérez García-Pando
932   C.: Variability in grain size, mineralogy, and mode of occurence of Fe in surface sediments of
933   preferential dust-source inland drainage basins: The case of the Lower Drâa Valley, S Morocco.
934   EGUsphere [preprint], https://doi.org/10.5194/egusphere-2023-1120, 2023.
935 Goryniuk M.C., Rivard B.A., and Jones B.: The Reflectance Spectra of Opal-A (0.5–25 Mm) from the
936   Taupo Volcanic Zone: Spectra That May Identify Hydrothermal Systems on Planetary Surfaces.
937   Geophysical Research Letters 31, 24, 2004. https://doi.org/10.1029/2004GL021481.
938 Goudie A.S. & Middleton N.J.: Desert dust in the global system. Springer, Heidelberg. ISBN 978-786 3-
939   540-32355-6, 288 pp, 2006.
940 Green R.O., Mahowald N., Ung C., Thompson D.R., Bator L., Bennet M., Zan J.: The earth surface
941   mineral dust source investigation: an earth science imaging spectroscopy mission. In: IEEE
942   Aerospace Conference Proceedings. IEEE Computer Society.
943   https://doi.org/10.1109/AERO47225.2020.9172731. 2020.
944 Groot Zwaaftink C.D., Arnalds Ó., Dagsson-Waldhauserova P., Eckhardt S., Prospero J.M., Stohl A.:
945   Temporal and spatial variability of Icelandic dust emissions and atmospheric transport, Atmos.
946   Chem. Phys., 17, 10865–10878, https://doi.org/10.5194/acp-17-10865-2017, 2017.
947 Horgan, B.H.N., Cloutis E.A., Mann P., and Bell J.F.: Near-Infrared Spectra of Ferrous Mineral Mixtures
948   and Methods for Their Identification in Planetary Surface Spectra. Icarus 234, 132–54, 2014.
949   https://doi.org/10.1016/j.icarus.2014.02.031.
950 Ibáñez J., Font O., Moreno N., Elvira J.J., Alvarez S., Querol X.: Quantitative Rietveld analysis of the
951   crystalline and amorphous phases in coal fly ashes. Fuel, 105: 314-317, 2013.

Jickells T.D., An Z.S., Andersen K.K., Baker A.R., Bergametti G., Brooks N., Cao J.J., Boyd P.W., Duce R.A., Hunter K.A., Kawahata H., Kubilay N., Laroche J., Liss P.S., Mahowald N., Prospero J.M., Ridgwell A.J., Tegen I., Torres R.: Global iron connections between desert dust, ocean biogeochemistry, and climate. Science, 308, 5718, 67-71. DOI: 10.1126/science.1105959, 2005.

Johnson M.S., Meskhidze N., Solmon F., Gassó S., Chuang P.Y., Gaiero D.M., Yantosca R.M., Wu S., Wang Y., Carouge C.: Modeling dust and soluble iron deposition to the South Atlantic Ocean. J. Geophys. Res., 115, D15202, doi:10.1029/2009JD013311, 2010.

Journet E., Balkanski Y., Harrison S.P.: A new data set of soil mineralogy for dust-cycle modeling. Atmos. Chem. Phys., 14, 8, 3801-3816, 2014.

Karanasiou A., Moreno N., Moreno T., Viana M., de Leeuw F., Querol X.: Health effects from Sahara dust episodes in Europe: Literature review and research gaps. Environ. Int. 47, 107–14, 2012.

Klose M. and Shao Y.: Large-eddy simulation of turbulent dust emission, Aeolian Res., 8, 49–58, https://doi.org/10.1016/j.aeolia.2012.10.010, 2013.

Kokaly R.F., Clark R.N., Swayze G.A., Livo K.E., Hoefen T.M., Pearson N.C., Wise R.A., Benzel W.M., Lowers H.A., Driscoll R.L.: USGS Spectral Library Version 7. U.S. Geological Survey Data Series 1035, 61 p, 2017. https://doi.org/10.3133/ds1035.

Kok J.F., Adebiyi A.A., Albani S., Balkanski Y., Checa-Garcia R., Chin M., Colarco P.R., Hamilton D.S., Huang Y., Ito A., Klose M., Li L., Mahowald N.M., Miller R.L., Obiso V., Pérez García-Pando C., Rocha-Lima A., Wan J.S.: Contribution of the world's main dust source regions to the global cycle of desert dust, Atmos. Chem. Phys., 21, 8169–8193, https://doi.org/10.5194/acp-21-8169-2021, 2021.

Kok, J.F., Storelvmo T., Karydis V.A., Adebiyi A.A., Mahowald N.M., Eva A.T., He C., Leung D.M.: Mineral dust aerosol impacts on global climate and climate change. Nat. Rev. Earth Environ. 4, 71–86, 2023. https://doi.org/10.1038/s43017-022-00379-5

Kylling A., Zwaaftink C.D.G., Stohl A.: Mineral Dust Instantaneous Radiative Forcing in the Arctic, Geophys. Res. Lett., 45, 4290–4298, 2018.

Laurent B.; Marticorena B.; Bergametti G.; Léon J.F., Mahowald N.M.: Modeling Mineral Dust Emissions from the Sahara Desert Using New Surface Properties and Soil Database J. Geophys. Res., 113, D14218, 2008.

Machiels L., Mertens G., Elsen J.: Rietveld Refinement strategy for Quantitative Phase analysis of Partially Amorphous zeolitized tuffaceous. GEOLOGICA BELGICA 13,3, 183-196, 2010.

Madsen I.C., Scarlett N.V.Y., Cranswick L.M.D., Lwin T.: Outcomes of the international union of crystallography commission on powder diffraction round robin on quantitative phase analysis: Samples 1a to 1h. J. Appl. Crystallogr., 34, pp. 409-426, 2001.

Mahowald N.M., Baker A.R., Bergametti G., Brooks N., Duce R.A., Jickells T.D., Kubilay N., Prospero J.M., Tegen I.: Atmospheric global dust cycle and iron inputs to the ocean, Global Biogeochem. Cy., 19(4), GB4025, doi:10.1029/2004GB002402, 2005.

Matsui H., Yamane M., Tonami T., Nagami T., Watanabe K., Kishi R., Kitagawa Y., Nakano M.: Theoretical study on gigantic effect of external static electric field application on nonlinear optical properties of 1,2,3,5-dithiadiazolyl π-radical dimer. Mater. Chem. Front., 2, 785– 790, DOI: 10.1039/C7QM00549K, 2018.

Meinander O., Dagsson-Waldhauserova P., Amosov P., Aseyeva E., Atkins C., Baklanov A., Baldo C., Barr S.L., Barzycka B., Benning L.G., Cvetkovic B., Enchilik P., Frolov D., Gassó S., Kandler K., Kasimov N., Kavan J., King J., Koroleva T., Krupskaya V., Kulmala M., Kusiak M., Lappalainen H.

997   K., Laska M., Lasne J., Lewandowski M., Luks B., McQuaid J.B., Moroni B., Murray B., Möhler
998   O., Nawrot A., Nickovic S., O'Neill N.T., Pejanovic G., Popovicheva O., Ranjbar K., Romanias M.,
999   Samonova O., Sanchez-Marroquin A., Schepanski K., Semenkov I., Sharapova A., Shevnina E.,
1000   Shi Z., Sofiev M., Thevenet F., Thorsteinsson T., Timofeev M., Umo N.S., Uppstu A., Urupina
1001   D., Varga G., Werner T., Arnalds O., Vukovic Vimic A.: Newly identified climatically and
1002   environmentally significant high-latitude dust sources. Atmos. Chem. Phys., 22, 11889–11930,
1003   https://doi.org/10.5194/acp-22-11889-2022, 2022.
1004   Möller R., Möller M., Kukla P.A., Scneider C., Römer W., Lehmkuhl F., Gudmundsson M.T.: Analyzing
1005   relationships between geochemical composition, spectral reflectance, broad-band albedo and
1006   thickness of supra-glacial tephra deposits from the eruptions of Eyafjallajökull and Grímsvötn
1007   volcanoes in 2010 and 2011. Am. Geoph. Union, Fall meeting, abstract #C13B-082, 2016.
1008   Möller R., Möller M., Kukla P.A., Schneider C.: Modulation of glacier ablation by tephra coverage from
1009   Eyjafjallajökull and Grímsvötn volcanoes, Iceland: an automated field experiment. Earth Syst.
1010   Sci. Data, 10, 53-60, https://doi.org/10.5194/essd-10-53-2018, 2018.
1011   Murray B.J., Carslaw K.S. and Field P.R.: Opinion: Cloud-phase climate feedback and the importance
1012   of ice-nucleating particles. Atmospheric Chemistry and Physics, 21, 2, 665-679.
1013   https://doi.org/10.5194/acp-21-665-2021, 2021.
1014   Oerlemans J., Giesen R., Van Den Broeke M.: Retreating alpine glaciers: Increased melt rates due to
1015   accumulation of dust (Vadret da Morteratsch, Switzerland). Journal of Glaciology, 55(192),
1016   729-736. doi:10.3189/002214309789470969, 2009.
1017   Ólafsson H., Furger M., Brümmer B.: The weather and climate of Iceland. Meteorologische Zeitschrift,
1018   16, 1, 005-008. https://doi.org/10.1127/0941-2948/2007/0185, 2007.
1019   Palacios D., Hughes D.H., García-Ruiz J.M. (eds.): European Glacial Landscapes. The last deglaciation.
1020   Elsevier. Amsterdam. ISBN 9780323918992, 2021.
1021   Panta A., Kandler K., Alastuey A., González-Flórez C., González-Romero A., Klose M., Querol X., Reche
1022   C., Yus-Díez J., Pérez García-Pando, C.: Insights into the single-particle composition, size,
1023   mixing state, and aspect ratio of freshly emitted mineral dust from field measurements in the
1024   Moroccan Sahara using electron microscopy, Atmos. Chem. Phys., 23, 3861–3885,
1025   https://doi.org/10.5194/acp-23-3861-2023, 2023.
1026   Pérez García-Pando C., Stanton M.C., Diggle P.J., Trzaska S., Miller R.L., Perlwitz J.P., Baldasano J.M.,
1027   Cuevas E., Ceccato P., Yaka P., Thomson M.C.: Soil dust aerosols and wind as predictors of
1028   seasonal meningitis incidence in Niger. Environ. Health Perspect. 122, 7679-686, 2014.
1029   Perlwitz J.P., Pérez García-Pando C., and Miller R.L.: Predicting the mineral composition of dust
1030   aerosols – Part 1: Representing key processes. Atmos. Chem. Phys., 15, 11593–11627,
1031   https://doi.org/10.5194/acp-15-11593-2015, 2015.
1032   Querol X.: The Occurrence and Distribution of Trace Elements in the Teruel Mining District Coals and
1033   their Behaviour during Coal Combustion. European Coal and Steel Community Project
1034   7220/ED/014, 1993.
1035   Querol X., Whateley M.K.G., Fernandez-Turiel J.L., Tuncali E.: Geological controls on the mineralogy
1036   and geochemistry of the Beypazari lignite, Central Anatolia, Turkey. Int. J. Coal. Geol., 33:255–
1037   271, 1997.
1038   Rampe E.B., Kraft M.D., Sharp T.G., Golden D.C., Ming D.W., and Christensen P.R.: Allophane Detection
1039   on Mars with Thermal Emission Spectrometer Data and Implications for Regional-Scale
1040   Chemical   Weathering   Processes.   Geology   40,   11,   995–98,   2012.
1041   https://doi.org/10.1130/G33215.1.

Raupach M.R., Gillette D.A., Leys J.F.: The effect of roughness elements on wind erosion threshold. J. Geophys. Res., 98, 3023-3029, 1993.

Rietveld H.M.: A profile refinement method for nuclear and magnetic structures. Journal of Applied Crystallography 2, 65–71, 1969.

Sanchez-Marroquin A., Arnalds O., Baustian-Dorsi K.J., Browse J., Dagsson-Waldhauserova P., Harrison A.D., Maters E.C., Pringle K.J., Vergara-Temprado J., Burke I.T., Mcquaid J.B., Carslaw K.S., Murray B.J.: Iceland is an episodic source of atmospheric ice-nucleating particles relevant for mixed-phased clouds. Science advances, 6, 26. DOI: 10.1126/sciadv.aba813, 2020.

Scarlett N. & Madsen I.: Quantification of phases with partial or no known crystal structures. Powder Diffraction, 21(4), 278-284, 2006.

Shao Y. and Lu H.: A simple expression for wind erosion threshold friction velocity, J. Geophys. Res.-Atmos., 105, 22437–22443, https://doi.org/10.1029/2000JD900304, 2000.

Shao Y. and Klose M.: A note on the stochastic nature of particle cohesive force and implications to threshold friction velocity for aerodynamic dust entrainment. Aeolian Res. 22, 123–125. https://doi.org/10.1016/j.aeolia.2016.08.004. 2016.

Shi Z.B., Krom M.D., Bonneville S.: Formation of Iron Nanoparticles and Increase in Iron Reactivity in Mineral Dust during Simulated Cloud Processing. Environ. Sci. Technol. 43, 6592-6596, 2009.

Shi Y., Liu X., Wu M.., ZhaoX., Ke Z. and Hunter B.: Relative importance of high-latitude local and long-range-transportated dust for Arctic ice-nucleating particles and impacts on Arctic mixed-phased clouds. Atmospheric Chemistry and Physics, 22, 4, 2909-2935. https://doi.org/10.5194/acp-22-2909-2022, 2022.

Sperazza M., Moore J.N., Hendrix M.: High-Resolution particle size analysis of naturally occurring very fine-grained sediment through laser diffractometry. J. Sediment. Res., 74(5):736-743, 2004.

Toby, B. H.: R factors in Rietveld analysis: How good is good enough?. Powder Diffr., 21, 67–70, https://doi.org/10.1154/1.2179804, 2006.

Thompson D.R., Babu K., Braverman A.J., Eastwood M.L., Green R.O., Hobbs J.M., Jewell J.B., Kindel B., Massie S., Mishra M.: Optimal estimation of spectral surface reflectance in challenging atmospheres. Remote Sens. Environ., 232, 111258, https://doi.org/10.1016/j.rse.2019.111258, 2019.

Thorsteinsson T., Gísladóttir G., Bullard J., McTainsh G.: Dust storm contributions to airborne particulate matter in Reykjavík, Iceland. Atmospheric Environment, 45, 32, 5924-5933. https://doi.org/10.1016/j.atmosenv.2011.05.023, 2011.

Thorpe M.T., Hurowitz J.A., Dehouck E.: Sediment geochemistry and mineralogy from a glacial terrain river system in southwest Iceland. Geochimica et Cosmochimica Acta. 263, 140-166. https://doi.org/10.1016/j.gca.2019.08.003, 2019.

TOPAS: TOPAS and TOPAS-Academic: an optimization program integrating computer algebra and crystallographic objects written in C++. J. Appl. Cryst. (2018). 51, 210-218, 2018.

Wada K., Arnalds O., Kakuto Y., Wilding L.P., Hallmark C.T.: Clay minerals of four soils formed in eolian and tephra materials in Iceland. Geoderma, 52, 3-4, 351-365. https://doi.org/10.1016/0016-7061(92)90046-A, 1992.

Wittmann M., Zwaaftink C.D.G., Schmidt L.S., Guðmundsson S., Pálsson F., Arnalds O., Björnsson H., Thorsteinsson T., Stohl A.: Impact of dust deposition on the albedo of Vatnajökull ice cap, Iceland. The Cryosphere, 11, 741-754, https://doi.org/10.5194/tc-11-741-2017, 2017.

Young R.A.: The Rietveld method. International Union of Crystallography. Oxford University Press, UK, 1993.

1087 Yus-Díez J., Pandolfi M., Alastuey A., González-Florez C., Escribano J., González-Romero A., Ivančič M.,
1088   Rigler M., Klose M., Kandler K., Panta A., Querol X., Reche C., Pérez García-Pando C.:
1089   Quantifying variations in multi-wavelength optical properties of freshly-emitted Saharan dust
1090   from the Lower Drâa Valley, Moroccan Sahara, in preparation, 2023.
1091 Zubko N., Munoz O., Zubko E., Gritsevich M., Escobar-Cerezo J., Berg M. J. and Peltoniemi J.: Light
1092   scattering from volcanic-sand particles in deposited and aerosol form. Atmospheric
1093   Environment, 215, 116813. https://doi.org/10.1016/j.atmosenv.2019.06.051, 2019.

1094
1095
1096
1097
1098
1099
1100
1101
1102
1103
1104
1105
1106
1107
1108
1109
1110
1111
1112
1113
1114
1115
1116
1117
1118
1119
1120
1121
1122
1123
1124
1125
1126
1127
1128
1129
1130

Figure captions:

Figure 1. Location of Iceland dust hotspots and samples. Black polygon marked the limits of Holuhraun lava field and in red are marked the area of the different dust hotspots in Iceland. Basemap: Imagery data from © Google Earth Pro v: 7.3.6.9345. Jökulsá á Fjöllum is marked as (a) and AVIRIS data flight images where used in the zoom in from Dyngjusandur (b) and Dyngjuvatn (c) for a more actualized vision of the lakes.

Figure 2. Examples of samples collected in Iceland from top sediments (a), fluvial sediments (a) and eolian ripples (b)).

Figure 3. Minimally dispersed particle size distribution (MDPSD) and fully dispersed particle size distribution (FDPSD) of top sediment, fluvial sediments and eolian ripple samples.

Figure 4. Mean median diameters of top sediments along the Jökulsá á Fjöllum river, according to the distance to the glacier moraine. The grey column indicates the location of the Holuhraun lava field and the red vertical line, a tributary channel of Jökulsá á Fjollum.

Figure 5. Particle size distributions of top sediment samples from different dust-emitting hotspots in Iceland as determined by MDPSD and FDPSD.

Figure 6. Contents of volcanic glass and crystalline minerals in top sediments, underlying fluvial sediments and eolian ripples from the Jökulsá á Fjöllum basin.

Figure 7. Reflectance spectra measured of surfaces in the field: (a) ripples in Iceland, (b) top sediments in Iceland, and (c) example spectra from Morocco. In (a) and (b), spectra are offset for clarity and are ordered by distance from the glacier.

Figure 8. Imaging spectrometer data from AVIRIS and analysed with Tetracorder (Clark et al., 2003, 2023). A) Grey scale image of 3 AVIRIS flight lines mosaicked for this study. The white circle if the primary study area and the grey rectangle is secondary sampling. B) Pyroxene composition map. The pyroxene dominant in the region are clinopyroxenes. C) Olivine composition map, which indicates the olivine are high iron content. However, in areas of significant Fe^{2+} bearing volcanic glass could bias this result. D) Fe^{2+} bearing minerals, which in those area is probably mostly due to volcanic glass. Note few locations mapped any Fe^{3+} bearing minerals. E) Map the EMIT 8 minerals with absorptions in the 2-2.5 micron spectral region. Only trace calcite and outcrops of chlorite/serpentine were found. F) Tetracorder map of water and significant water bearing sediments. Where strong water absorptions are seen, detection of other minerals is difficult and usually blank in panels B-E.

Figure 9. Contents of volcanic glass and crystalline minerals in top sediments, underlying fluvial sediments and eolian ripples from different dust-emitting hotspots. Dyn: Dyngjusandur, Dvt: Dyngjuvatn, Lan: Landeyjarsandur, Mýr: Mýrdalsandur, Ska: Skaftarsandur, Mæl: Mælifellsandur, Hgv: Hagavatn.

Figure 10. Average percentage of FeS, FeM, FeD and FeA for the Jökulsá á Fjöllum basin and average amount of each Fe mode of occurrence according to the total content of Fe.

Figure 11. Average percentage of FeS, FeM, FeD and FeA for Dyn: Dyngjusandur, Dvt: Dyngjuvatn, Lan: Landeyjarsandur, Mýr: Mýrdalssandur, Mæl: Mælifellsandur, Hvt: Hagavatn and Ska: Skaftarsandur and average amount of each Fe mode of occurrence according to the total content of Fe of the same dust emitting sources.

Figure 12. Trends in infrared spectral features with distance from the glacier. (a) The depth of a broad absorption feature at 1.035 μm (BD1035) due to Fe^{2+} in volcanic glass and/or pyroxene. (b) The depth of an absorption feature at 1.9 μm (BD1900) due to H_2O. (c) The depth of an absorption feature at 2.21 μm (BD2210) due to Si-OH or Al-OH. (d) The albedo (brightness), calculated as the mean reflectance at 1.62-1.63 μm. Black points are spectra of ripples, and gray are spectra of top sediments.

Figure 13. SEM microphotographs of collected dust samples: a) Particles from a top sediment sample from Dyngjusandur showing dispersed particles. b) Particles from a top sediment sample from the lowlands of M'Hamid, Morocco (see González-Romero et al., 2023), showing finer particle size and a high degree of agglomeration. c) Particles from underlying fluvial sediments, from Dyngjusandur, showing a large particle size and fresh volcanic glassy material. d, e, and f) Samples of top sediments (d and e) from

1179 Dyngjuvatn, showing abundant elongated particles and agglomerates of particles derived from the
1180 breaking of larger pumice particles. g) Image showing particles with magnetite inclusions.
1181 **Figure 14.** Average amount of each Fe mode of occurrence for top sediment JaF: Jökulsá á Fjöllum top sediment
1182 average, Sediment JaF: Jökulsá á Fjöllum sediment average, Ripple JaF: Jökulsá á Fjöllum ripples
1183 average, Dyn: Dyngjusandur, Dvt: Dyngjuvatn, Lan: Landeyjarsandur, Mýr: Mýrdalssandur, Mæl:
1184 Mælifellsandur, Hvt: Hagavatn, Ska: Skaftarsandur, Crust S: Average crust from Sahara, Sediment S:
1185 Average sediment from Sahara and Ripple S: Average ripple from Sahara and average percentage of
1186 FeS, FeM, FeD and FeA normalised by the amount of FeT.
1187 **Figure 15.** Conceptualization of the origin, transport, sedimentation and emission of dust emitting sources,
1188 sediments and dust along Iceland, using the example of the Jökulsá á Fjöllum basin. t1: The glacier feeds
1189 the fluvial systems with fine particles that are transported and size segregated along the basin, t2: in
1190 flat areas or if a volcanic eruption forms a dam, the sediments deposits, t3: under favourable conditions
1191 the dust emission occurs in different parts of the basin by saltation and aerodynamic entrainment.
1192 **Figure 16.** Example of how particles, mainly volcanic glass with minor proportions of pyroxenes, feldspars and
1193 some iron oxides are transported, segregated and after drying and under favourable conditions,
1194 aerodynamic entrainment and saltation bombardment.
1195

1196

1197

1198

1199

1200

1201
1202
1203
1204
1205
1206
1207
1208
1209
1210
1211
1212
1213
1214
1215
1216
1217
1218
1219
1220
1221
1222

1223

1224   **Figure 1.**
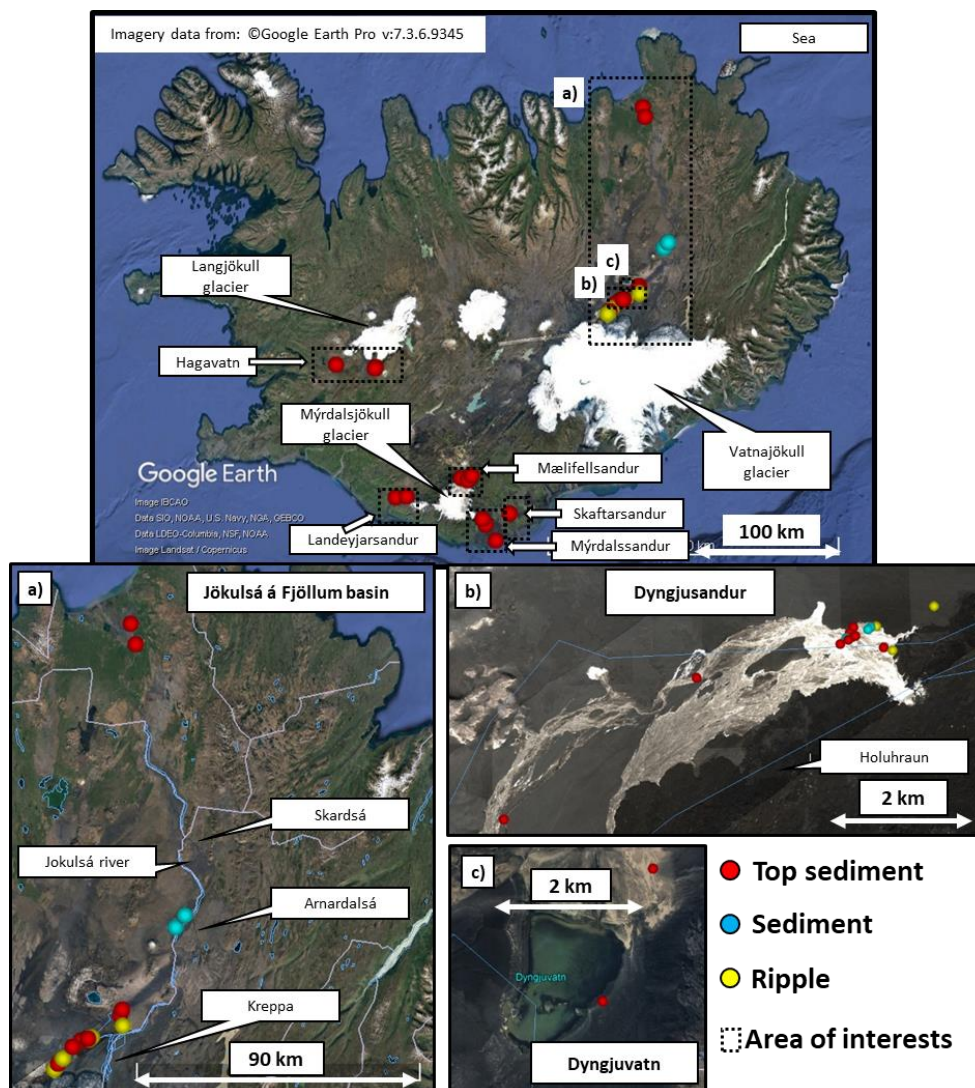
1225

1226 **Figure 2.**

1227
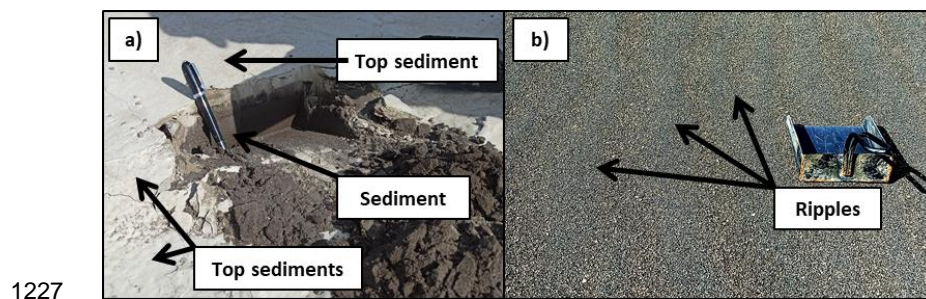
1228   **Figure 3.**
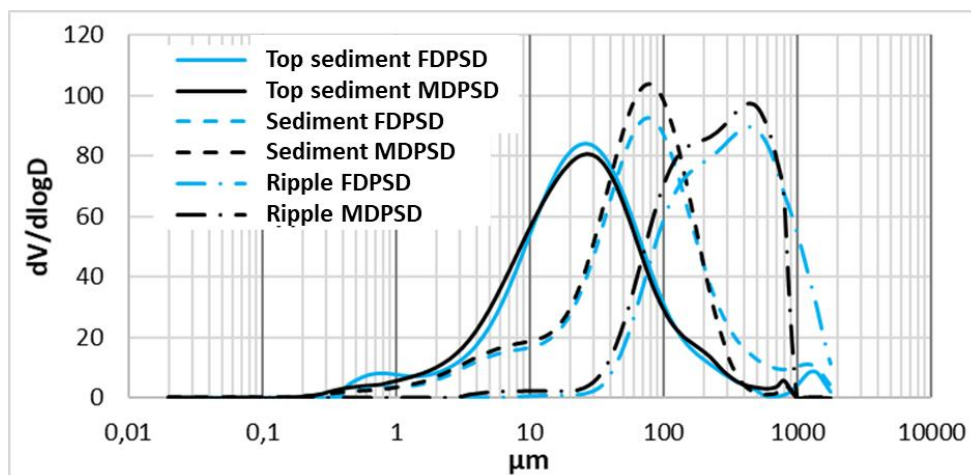
1229

1230   **Figure 4.**
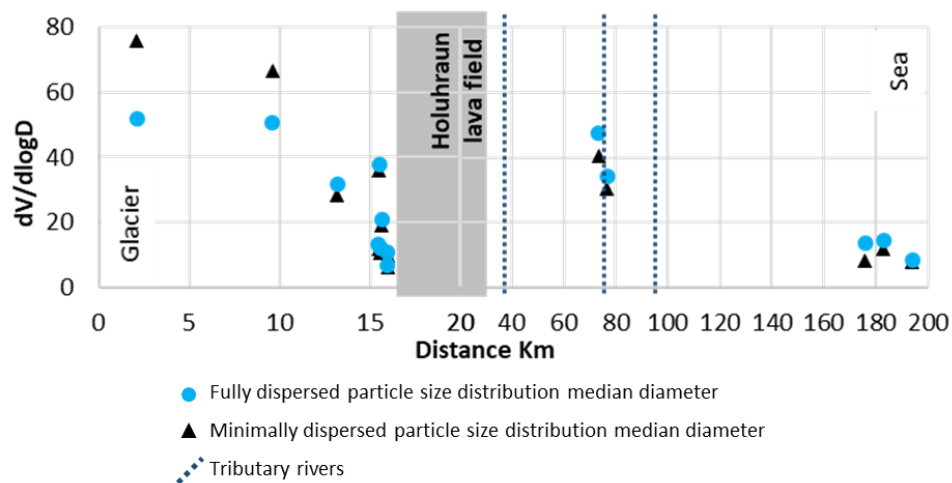
1231

1232   **Figure 5.**
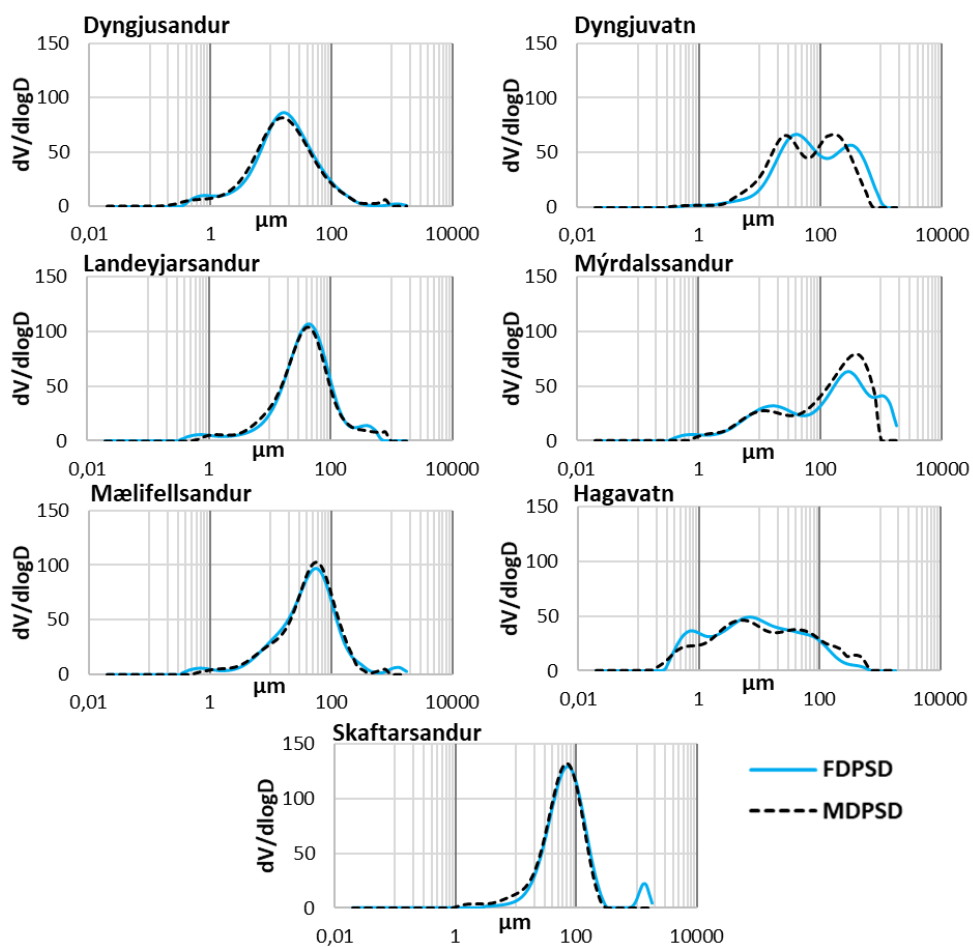
1233

1234   **Figure 6.**
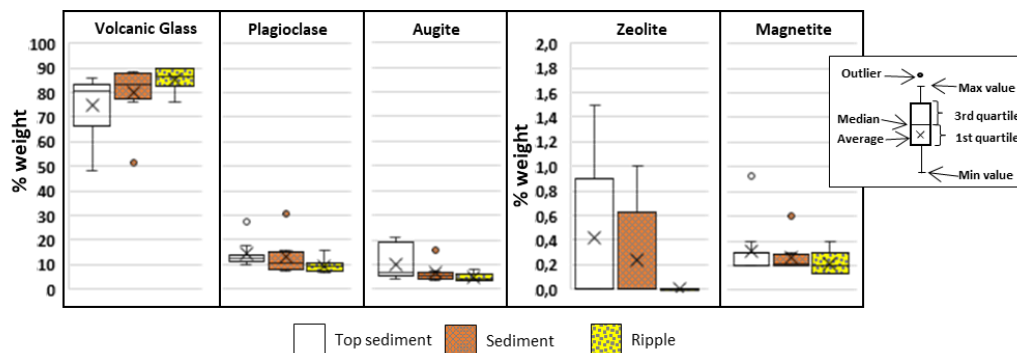
1235

1236   **Figure 7.**
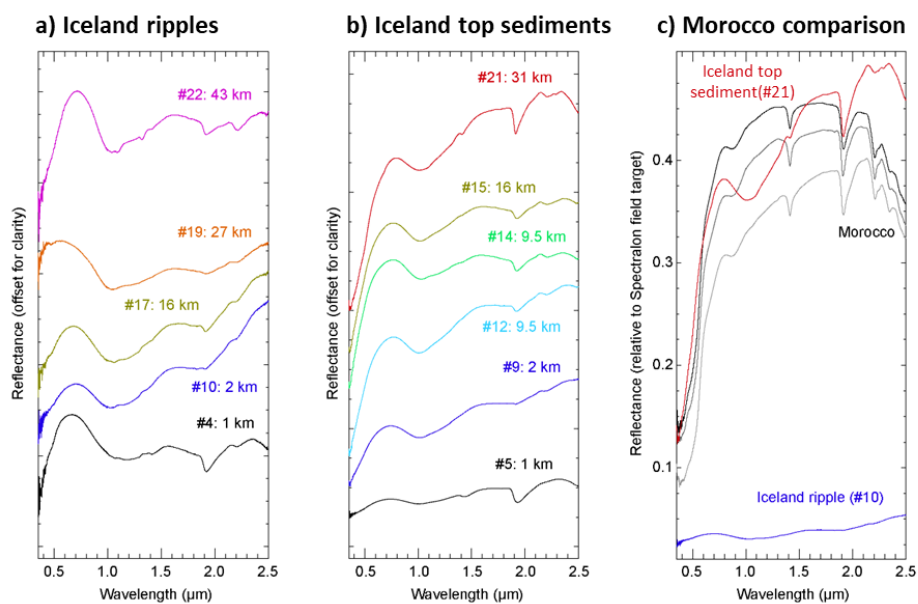
1237

1238   **Figure 8.**

1239

1240   **Figure 9.**
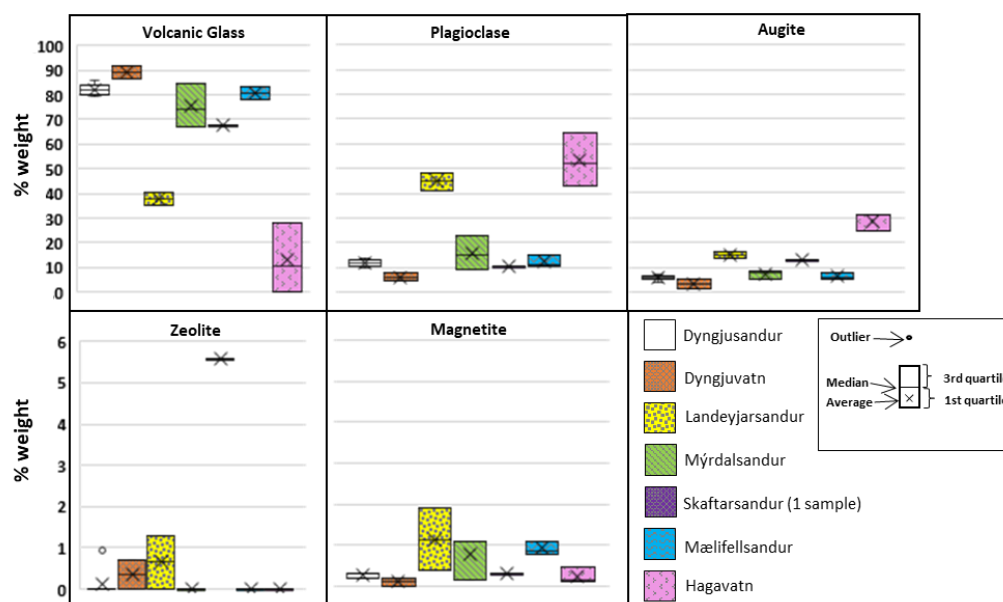
1241

1242   **Figure 10.**
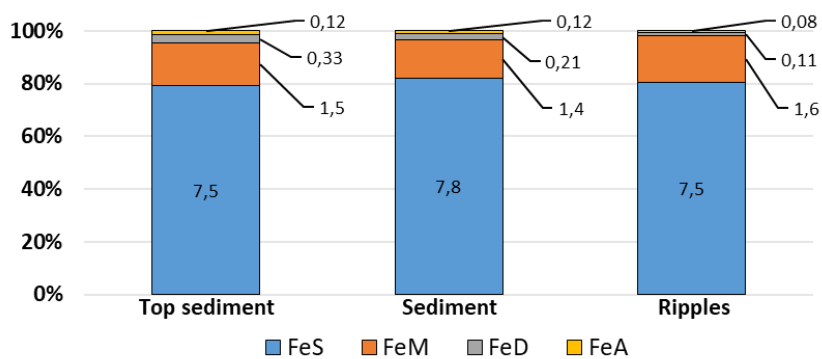
1243

1244   **Figure 11.**

1245
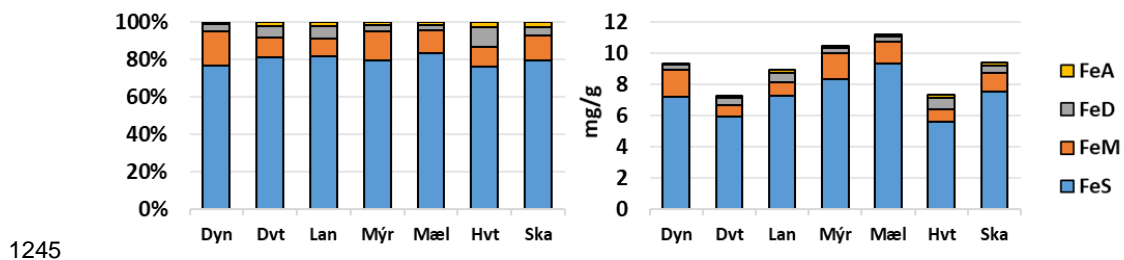
1246   **Figure 12.**
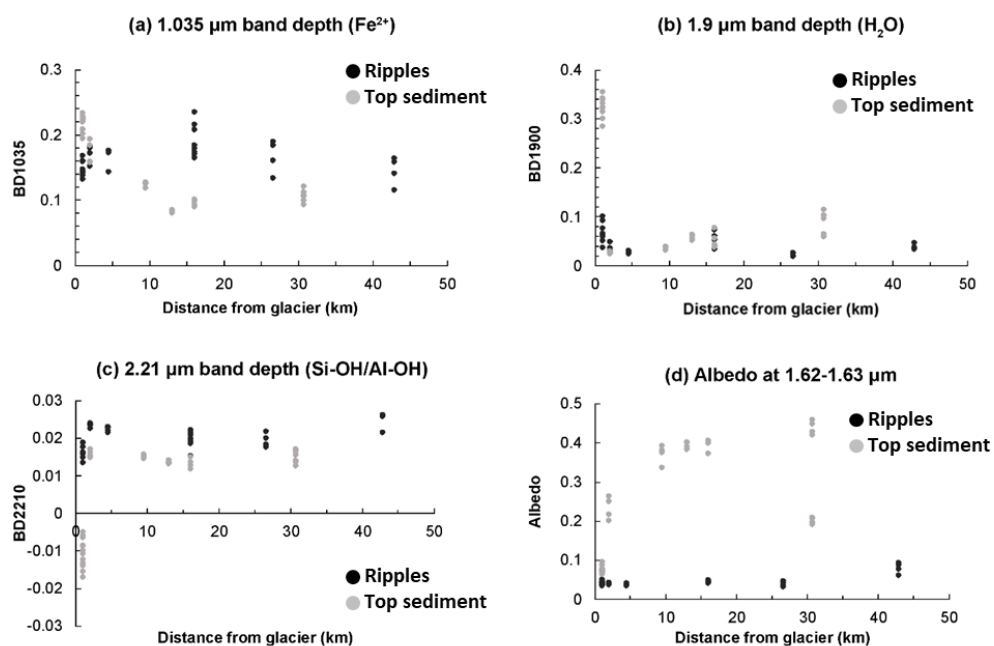
1247

1248   **Figure 13.**
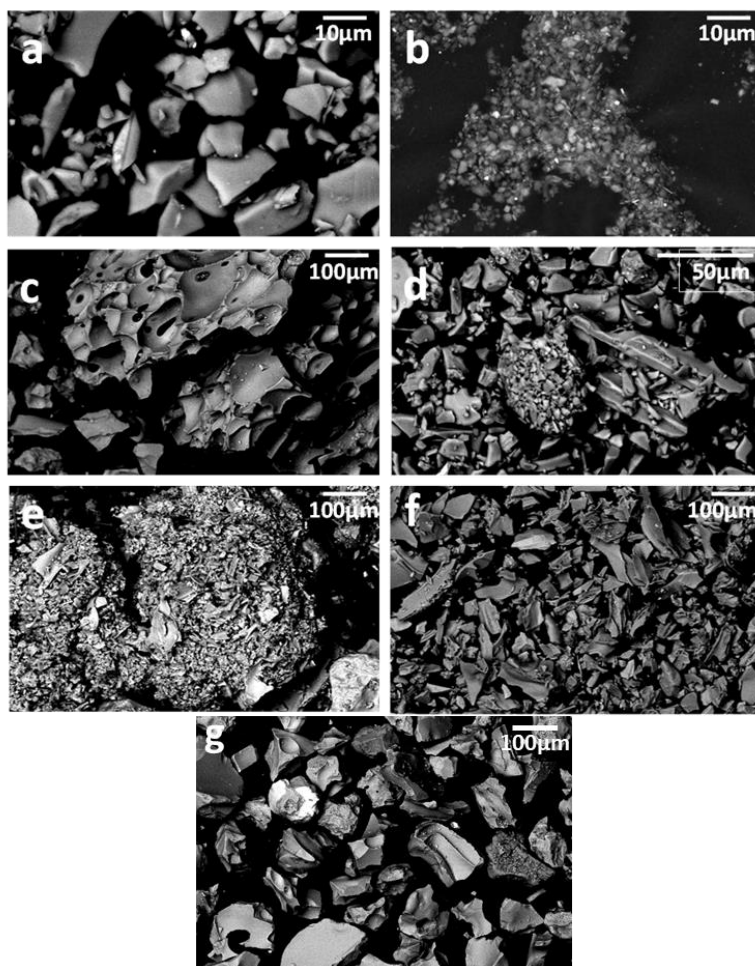
1249

1250 **Figure 14.**
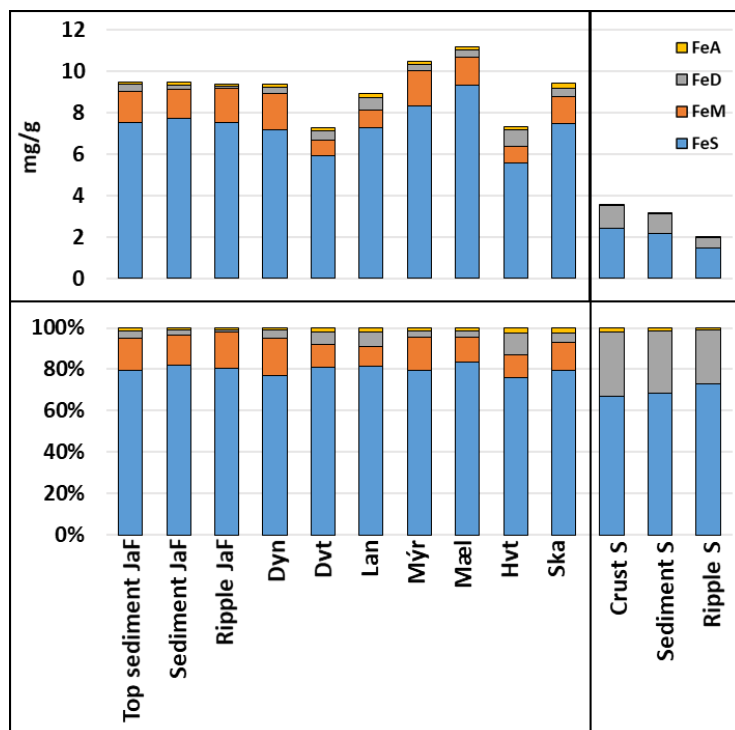
1251

1252   **Figure 15.**
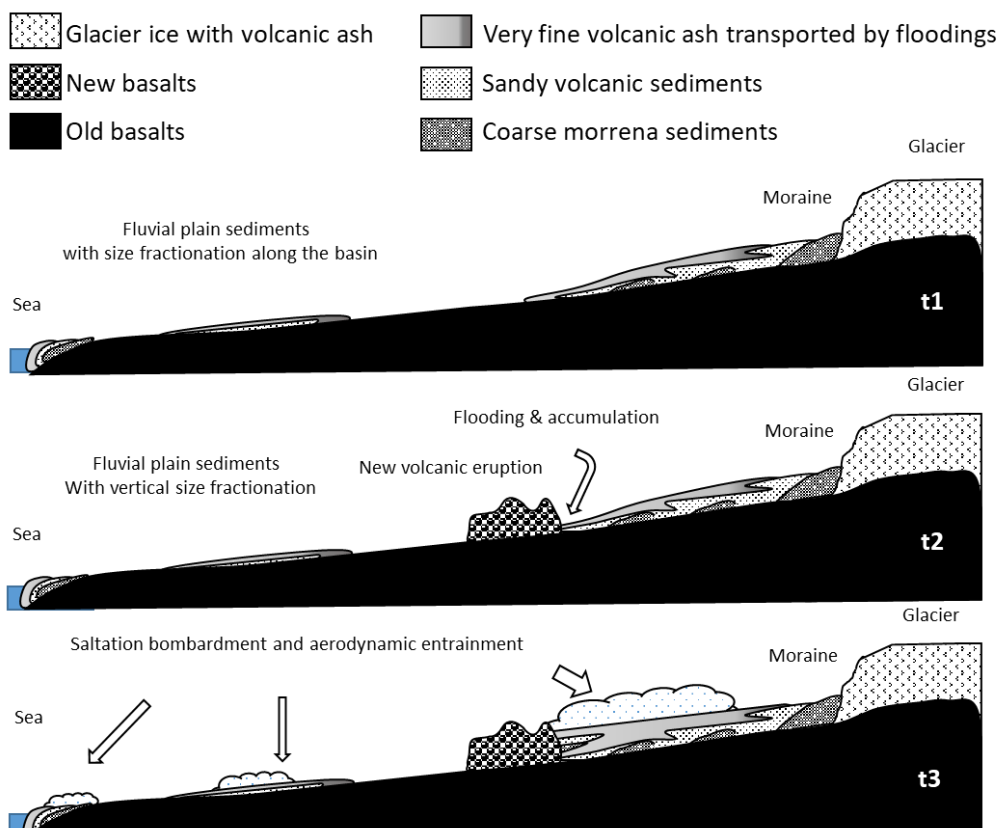
1253

1254  **Figure 16.**
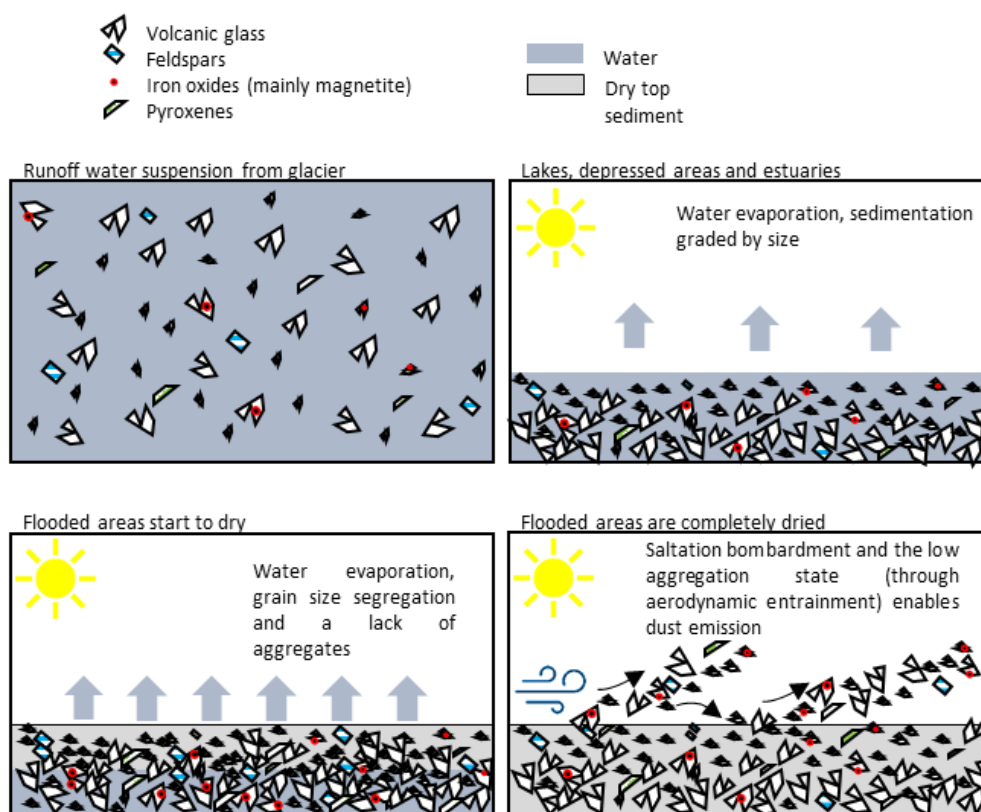
1255

1256 **Table 1.** Mean median diameters, standard deviation, min., max. (µm) of top sediments, underlying fluvial
1257   sediments and eolian ripples from the Jokulsá á Fjöllum basin, for minimally dispersed particle size
1258   distribution (MDPSD) and fully dispersed particle size distribution (FDPSD). *Extracted from González-
1259   Romero et al. (2023).

Surface type	Nº samples	MDPSD (Mean of medians±sd [Min,Max])	FDPSD (Mean of medians±sd [Min,Max])
All samples	31	107±129 [6.4,502]	133±174 [6.8,738]
Top sediments	15	32±20 [6.4,76]	31±15 [6.8,52]
Sediments	8	74±49 [7.9,158]	102±91 [7.3,284]
Ripples	8	280±144 [114,502]	354±203 [133,738]

1260
1261
1262
1263
1264
1265
1266
1267
1268
1269
1270
1271
1272
1273
1274
1275
1276
1277
1278
1279
1280
1281
1282
1283
1284
1285
1286
1287
1288
1289
1290
1291

1292   **Table 2.** Mean median diameter, standard deviation, min., max. (µm) of top sediment sediments from minimally
1293   dispersed particle size distribution (MDPSD) and fully dispersed particle size distribution (FDPSD).
1294   *Median top sediment MDPSD and FDPSD extracted from González-Romero et al. (2023).

Location	Nº samples	MDPSD (Mean of medians±sd [Min,Max])	FDPSD (Mean of medians±sd [Min,Max])
Iceland	23	55±62 [3.3,234]	56±69 [2.9,263]
Dyngjusandur	9	24±19 [6.4,66]	24±15 [6.8,51]
Dyngjuvatn	2	100±105 [26,175]	146±156 [36,256]
Landeyjarsandur	2	41±4.9 [37,44]	43±12 [38,48]
Mýrdalssandur	3	163±92 [59,234]	147±108 [49,263]
Mælifellsandur	3	48±13 [40,63]	46±9.5 [37,59]
Hagavatn	3	26±26 [3.3,55]	16±12 [2.9,26]
Skaftarsandur	1	63	72

1295

1296

1297

1298

1299

1300

1301

1302

1303

1304

1305

1306

1307

1308

1309

1310

Table 3. Mean median diameters, standard deviation, min., max. (μm) of top sediments, underlying fluvial sediments and eolian ripples from the Jokulsá á Fjöllum basin and Sahara Desert, for minimally dispersed particle size distribution (MDPSD) and fully dispersed particle size distribution (FDPSD). *Extracted from González-Romero et al. (2023).

Location	Surface type	Nº samples	MDPSD (Mean of medians±sd [Min,Max])	FDPSD (Mean of medians±sd [Min,Max])
Jökulsá á Fjöllum	All samples	31	107±129 [6.4,502]	133±174 [6.8,738]
Jökulsá á Fjöllum	Top sediments	15	32±20 [6.4,76]	31±15 [6.8,52]
Jökulsá á Fjöllum	Sediments	8	74±49 [7.9,158]	102±91 [7.3,284]
Jökulsá á Fjöllum	Ripples	8	280±144 [114,502]	354±203 [133,738]
Iceland	Top sediments	23	55±62 [3.3,234]	56±69 [2.9,263]
Dyngjusandur	Top sediments	9	24±19 [6.4,66]	24±15 [6.8,51]
Dyngjuvatn	Top sediments	2	100±105 [26,175]	146±156 [36,256]
Landeyjarsandur	Top sediments	2	41±4.9 [37,44]	43±12 [38,48]
Mýrdalssandur	Top sediments	3	163±92 [59,234]	147±108 [49,263]
Mælifellsandur	Top sediments	3	48±13 [40,63]	46±9.5 [37,59]
Hagavatn	Top sediments	3	26±26 [3.3,55]	16±12 [2.9,26]
Skaftarsandur	Top sediments	1	63	72
Sahara*	Top sediments (erg Smar)	8	131±89 [21, 320]	7.0±3.0 [2.7,10]
Sahara*	Sediments (erg Smar)	2	115±45 [83,147]	22±23 [5.8,39]
Sahara*	Ripples (erg Smar)	4	286±49 [244,355]	263±32 [239,308]

Table 4. Fe mode of occurrence from different locations and types of sample. The content of FeT is in %wt and for every mode of occurrence it is in % of the total Fe content. FeA: content of readily exchangeable Fe, FeD: Fe content from hematite, goethite and pyrite, FeM: Fe content from magnetite, FeS: Fe content from non Fe minerals as Fe-silicates and volcanic glass.

Location	Type of sample	FeT %wt	FeA %	FeD %	FeM %	FeS %
Jökulsá á Fjöllum	Top sediment	9.5±0.39	1.3±0.39	3.5±1.5	16±5.4	79±6.5
Jökulsá á Fjöllum	Sediment	9.5±0.43	1.2±0.44	2.2±1.4	15±7.8	82±8.7
Jökulsá á Fjöllum	Ripples	9.4±0.41	0.85±0.22	1.2±0.41	18±2.4	80±2.4
Dyngjusandur	Top sediment	9.4±0.21	1.2±0.45	3.6±1.8	18±4.6	77±6.7
Dyngjuvatn	Top sediment	7.3±2.6	2.1±0.64	7.0±5.1	10±3.5	81±2.3
Landeyjarsandur	Top sediment	8.9±0.54	1.8±0.67	7.2±2.1	9.5±3.2	81±5.9
Mýrdalssandur	Top sediment	11±0.41	1.4±0.33	3.2±1.4	16±1.9	79±2.3
Skaftarsandur	Top sediment	9.4±NA	2.6±NA	4.4±NA	13±NA	80±NA
Mælifellsandur	Top sediment	11±0.48	1.3±0.46	3.0±0.77	12±3.8	83±4.8
Hagavatn	Top sediment	7.4±1.5	2.7±1.0	10±2.2	11±2.4	76±4.4
Sahara	Top sediment	3.6±0.71	1.9±0.55	31±2.3	Negligible	67±2.4
Sahara	Sediment	3.2±0.47	1.4±0.55	30±3.0	Negligible	68±2.7
Sahara	Ripples	2.0±0.44	1.0±0.54	26±5.8	Negligible	73±5.9